10

Alfvén Waves in the Earth's Magnetosphere

Andrew N. Wright[1], Michael D. Hartinger[2,3], Kazue Takahashi[4], and Tom Elsden[1]

ABSTRACT

The environment surrounding the Earth that is dominated by the terrestrial magnetic field is called the magnetosphere. It comprises a highly structured magnetic field and plasma distribution. Transient events in the magnetosphere can arise from interaction with the solar wind or internal reconfigurations via reconnection, which are a natural source of magnetohydrodynamic (MHD) waves. We shall focus on the global scale waves that have wavelengths similar to the size of the magnetosphere. The different wave modes naturally couple to each other due to the structured nature of the magnetosphere. In particular, coupling of the fast magnetoacoustic mode and the Alfvén mode is common throughout the magnetosphere and is used in magneto-seismology studies. Alfvén waves can also be excited when unstable particle distributions arise. Whatever the source of the Alfvén waves, they are an agent for carrying field-aligned currents which can become particularly intense near the Earth. Consideration of these strong currents requires a two-fluid or kinetic treatment, which indicates the need for a region (at altitudes of 1–2 R_e) where electrons are accelerated to kiloelectron volt energies and can produce optical auroral emissions. Alfvén waves can also modify the ionosphere and induce ground currents, both of which have important implications for space weather. We review recent advances including the theory of Alfvén wave excitation in a 3D equilibrium and particle acceleration.

10.1. INTRODUCTION

The scope of this review is large-scale Alfvén waves within the Earth's magnetosphere with wavelengths of the order of the size of the magnetosphere itself (10 R_e). Specifically, we focus on advances over the last decade and cover theoretical and observational progress. For a description of developments outside of this period, we refer the reader to previous review articles and describe them briefly at the end of this section. We begin with a preamble giving a concise summary of the structure of the magnetosphere and relevant terminology for those unfamiliar with these details. Section 10.1.2 of the review by Nakariakov et al. (2016) provides an alternative overview of the magnetosphere with similar motivation. The textbook by Kivelson and Russell (1995) also provides a summary of magnetospheric structure as well as relevant plasma physics.

10.1.1. Structure of the Earth's Magnetosphere

Figure 10.1(a) shows a cartoon of the Earth's magnetosphere, which comprises the region surrounding the Earth that is permeated by terrestrial magnetic field lines. The magnetosphere forms a protective magnetic bubble

[1] *Department of Mathematics and Statistics, University of St Andrews, St Andrews, UK*

[2] *Department of Earth, Planetary, and Space Sciences, University of California Los Angeles, Los Angeles, CA, USA*

[3] *Space Science Institute, Boulder, CO, USA*

[4] *The Johns Hopkins University Applied Physics Laboratory, Laurel, MD, USA*

that shields the Earth from the fast-flowing solar wind in which it stands. It extends about 10 R_e toward the Sun. The solar wind flow is supersonic at 1 AU, so a bow shock forms upstream of the magnetosphere (not shown in Figure 10.1). The region between the bow shock and the magnetosphere contains subsonic shocked solar wind and is called the magnetosheath.

The solar wind carries magnetic field and plasma from the Sun, which bathes the magnetosphere. The boundary separating the Earth's magnetic field from that of the solar wind is called the magnetopause, and the dominant interaction between these magnetic fields is through reconnection: at the dayside magnetopause the terrestrial field is directed northward. When the solar wind field is directed southward it can reconnect with the terrestrial field on the dayside, forming 'open' field lines that have one end connected to the Earth and extend out into the solar wind.

As the field is frozen into the fast-flowing solar wind plasma, the open field lines are drawn out into a long magnetotail on the nightside. The northern half of the tail has a magnetic field directed earthward, which is opposite to that of the southern half. As the tail magnetic field is oppositely directed across the center of the tail, further reconnection can occur in the tail and lead to the formation of 'closed' field lines (that are solely connected to the Earth) and field lines that are connected to the solar wind, and exiting the tail in the anti-sunward flowing solar wind.
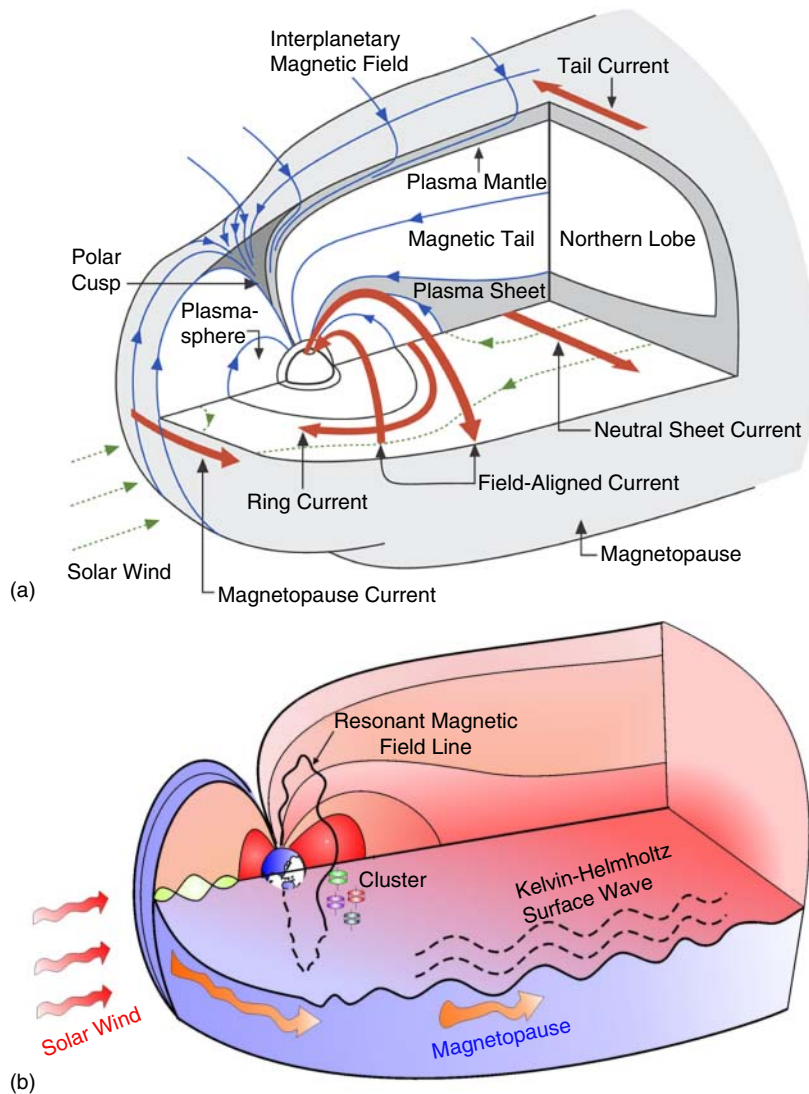
Figure 10.1 (a) The structure of the Earth's magnetosphere (Nakariakov et al. (2016) / Springer Nature). (b) Excitation of waves in the magnetosphere by the solar wind (from the ESA/Cluster website, https://sci.esa.int/web/cluster/-/41208-cluster-helps-reveal-how-the-sun-shakes-the-earth-s-magnetic-field).

The newly formed closed magnetotail field lines move earthward under magnetic stresses and adopt a dipole-like configuration as they approach the Earth. As more closed flux is added from the tail, these field lines move around the flanks and back to the dayside, where they, once again, reconnect with the solar wind magnetic field. Thus, there is a global convection of magnetic flux and plasma within the magnetosphere, and it is important to understand the density variations this produces.

The open magnetic field lines that are stretched anti-sunward form the outer part of the magnetotail. The volume of these flux tubes increases dramatically as they are stretched, and so they have a very low plasma density. This region is known as the tail 'lobe' and has a high Alfvén speed. When reconnection occurs in the tail, the newly formed closed field lines reduce their volume as they move earthward, which leads to the center of the magnetotail having a much higher density than the tail lobes. It is known as the 'plasma sheet' and has a low Alfvén speed compared to the lobes. As we move northward from the plasma sheet to the lobe, there is a rapid change in density and Alfvén speed, and this region is termed the plasma sheet boundary layer (PSBL).

All the terrestrial field lines involved in the global convection of plasma described earlier will connect to the Earth at relatively high latitudes, as they need to map to the outer parts of the magnetosphere to undergo reconnection with the solar wind field. Field lines that connect to the Earth at low latitudes will not be part of this reconnection cycle. They will remain connected to, and co-rotate with, the Earth. They are in equilibrium with the ionospheric plasma and so have a significantly higher density and lower Alfvén speed compared to neighboring open field lines. The region of closed low-latitude field lines is known as the plasmasphere and is shown as the dark red region close to the Earth in Figure 10.1(b). The outer boundary of the plasmashere is called the plasmapause, and the Alfvén speed changes abruptly across it.

Many particles on closed dipole-like field lines gyrate about the magnetic field and undergo various guiding center drifts. Conservation of the first adiabatic invariant leads to magnetic mirroring as the particles spiral around field lines and encounter enhanced field strengths as they approach Earth. These particles are effectively trapped on the field lines and bounce back and forth across the equator unless other processes come into play. These regions of trapped particles are known as the radiation belts or Van Allen belts. Such particles will also exhibit curvature and gradient drifts. For ions, this results in westward procession, while electrons move eastward and lead to a net current encircling the Earth called the ring current. (See the westerly directed ring current in Figure 10.1(a).)

10.1.2. MHD Waves in the Magnetosphere

The nonuniform Alfvén speed of the magnetosphere allows for a rich variety of wave behavior. The simplest way to discuss many of the large-scale waves we observe is through magnetohydrodynamics (MHD). In particular, we shall focus on the fast magnetoacoustic and the Alfvén modes.

Historically, the waves we shall consider were referred to as Geomagnetic Micropulsations, and were first observed as fluctuations in ground magnetometer data. Jacobs et al. (1964) introduced a classification system based on whether the fluctuations have a continuous sinusoidal nature (denoted by Pc, for continuous pulsation) or an irregular nature (Pi, for irregular pulsation). Within each category there are further subdivisions to denote the period, or characteristic time scale, of the pulsation. Of particular relevance to this review is the Pi2 category. These waves have an irregular time dependence with a characteristic timescale in the range of 45–150 s, and are found to originate mainly on the nightside. The other important class of waves we consider is the Pc5 category. These are continuous oscillations with a period in the range of 150–600 s and are found most frequently outside the plasmapause. They are the lowest frequency waves of the magnetosphere and are also referred to as ULF (Ultra-Low Frequency) waves.

Much of the theory of the generation of ULF waves has assumed an axisymmetric equilibrium with wave perturbations that vary sinusoidally with the azimuthal coordinate, as characterized by the azimuthal wavenumber, m. We shall see that "Low-m" (typically $m < 10$) and "High-m" (typically $m > 20$) waves have very different generation mechanisms and properties. Even though modeling of these waves has progressed beyond axisymmetric equilibria (so the use of an azimuthal wavenumber has limited applicability), the terms Low-m and High-m are still used in an informal manner to distinguish between the two types of waves.

Low-m Alfvén Waves

The source of waves in the magnetosphere can be traced back to the solar wind. The solar wind is fast-flowing, so there is an abundance of free energy that may be tapped. For example, the flanks of the magnetopause can be susceptible to the Kelvin-Helmholtz instability (see Figure 10.1(b)). There are also plasma density variations in the solar wind that can give rise to a fluctuating dynamic pressure on the magnetopause. Sometimes this can give a sudden smack to the magnetosphere, and other times it can provide a continual buffeting of the boundary.

The fast mode is important as it can transport solar wind energy away from the magnetopause and into the magnetosphere. The most easily excited fast waves in the global magnetospheric system are the natural fast eigenmodes. Some of these can be characterized as 'cavity' modes. For example, the abrupt change in Alfvén speed across the plasmapause can lead to effective trapping of fast wave energy in the plasmaspheric cavity. It is also possible to get cavity-like fast modes on the dayside that stand radially between the magnetopause and an inner turning point or the plasmapause. This is depicted as the light green wave in Figure 10.1(b).

The fast eigenmodes on the flanks are free to propagate into the magnetotail, so they are better described as waveguide modes. Both fast cavity and waveguide modes can couple to Alfvén waves on closed field lines. The Alfvén waves have a standing structure between the two ionospheric footpoints and have natural frequencies and harmonics like those of a clamped string under tension. Given that the length of the field lines and Alfvén speeds vary throughout the magnetosphere, the frequency of the Alfvén waves will vary too.

In a simple axisymmetric model of the dipole-like field line region, coupling of the fast mode to the Alfvén mode is most efficient for low azimuthal wavenumbers ($3 < m < 6$). The Alfvén waves excited have plasma displacement, velocity, and magnetic field perturbations aligned with the azimuthal direction. They are termed 'toroidal' Alfvén waves, and their frequency $\omega_A(L)$ is a function of L-shell. (Here, the L-shell parameter L is the radial distance to the field line in the equatorial plane and is measured in units of Earth radii, R_e.)

Resonant excitation of low-m Alfvén waves occurs on the L-shell, where the toroidal $\omega_A(L)$ matches the fast cavity or waveguide frequency (Chen & Hasegawa, 1974; Southwood, 1974); see the resonant field line in Figure 10.1(b). These are the lowest frequency Alfvén waves of the magnetosphere and typically have periods of 150–600 s. They are classified as Ultra-Low-Frequency (ULF) waves or Pc5 waves (band 5 of the continuous pulsation classification scheme). Low-m resonantly driven Alfvén waves on closed field lines are often referred to as Field Line Resonances (FLRs).

When low-m Alfvén waves are excited impulsively (rather than resonantly), they can become established across a broad range of L-shells. After the impulse has passed, the Alfvén waves will oscillate at their natural frequency, $\omega_A(L)$. Even if the waves on all L-shells start with their oscillations being in-phase, as time increases, they will drift further and further out of phase with their neighbors. This process is known as phase mixing, and is characterized by the development of a wavelength across field lines, called the phase-mixing length. For an ideal axisymmetric system, the phase-mixing length in the

equatorial plane in the radial direction will be

$$L_{ph} = \frac{2\pi R_e}{|d\omega_A(L)/dL|t}, \tag{10.1}$$

so reduces with time as t^{-1} (Mann et al., 1995).

Magnetotail and Nightside Alfvén Waves

The northern half of the magnetotail is shown in Figure 10.2, and Alfvén waves also exist here. The structure of the magnetotail formed by a distant downtail reconnection site is shown. (The distant reconnection site is to the far right of the figure, so it is not shown.) The low Alfvén speed plasma sheet (centered on the dashed line) transitions, via the plasma sheet boundary layer (PSBL), to the high Alfvén speed lobe. Reconnection can also occur in an explosive fashion at a near-earth reconnection site, which reconnects significant tail flux in a short time. This process is known as a substorm and releases solar wind energy stored in the stretched magnetic field.

The transient nature of a substorm can cause the magnetotail to reverberate with MHD waves. Fast waves can be released (labelled (1) in Figure 10.2), and these can become trapped in the low Alfvén speed plasma sheet as they propagate earthward, in what is known as the tail waveguide model. The fast mode is able to excite Alfvén waves in the PSBL and the lobe through coupling similar to that of the low-m Alfvén waves on closed field lines. Unlike the low-m Alfvén waves (which have a standing structure along the closed field line), the Alfvén waves excited in the PSBL and lobe (labelled (2) in Figure 10.2) propagate along the field line. The most efficient coupling occurs in the PSBL, with smaller Alfvén waves in the lobe as the fast mode is evanescent there due to the higher Alfvén speed.

The large gradient in Alfvén speed in the PSBL leads to Alfvén wave phase mixing (3) and the generation of strong field-aligned currents there. The current in the PSBL is larger than that in the lobe (4) and is carried mainly by
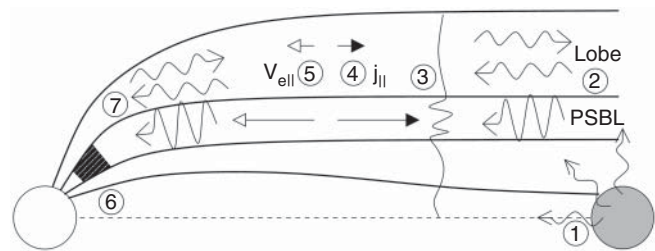
Figure 10.2 Schematic of MHD waves in the magnetotail waveguide (Wright & Allan (2008) /John Wiley & Sons). Alfvén waves excited in the Plasma Sheet Boundary Layer (PSBL) undergo phase mixing which produces strong field-aligned currents carried by energetic electrons that can generate optical auroral emissions in the ionosphere.

the motion of electrons along field lines (5). The currents are intensified further by the converging field geometry on approaching Earth, which leads to the formation of an electron acceleration region at altitudes of 1–2 R_e (6). A proper treatment of electron energization goes beyond single-fluid MHD. The acceleration of electrons can remove substantial energy from the Alfvén wave, resulting in weak reflection from the ionosphere. This is in contrast to the lobe, where the current is much weaker and allows the possibility of incident and reflected Alfvén waves superposing locally to give a standing wave (7).

The precipitation of energetic electrons associated with strong field-aligned currents in the ionosphere can give rise to optical auroral emissions modulated at the wave frequency. This is also true for Alfvén waves on closed field lines. Describing the energization of these electrons requires the use of two-fluid MHD or kinetic theory.

Besides the possibility of exciting Alfvén waves in the magnetotail through fast mode coupling, there exists the possibility of producing them more directly. A substorm will produce strong earthward flows of reconnected flux that give an impulsive push to the near-earth dipole-like field lines on the nightside. This can be an effective way of exciting the plasmapsheric cavity modes, which then couple to Alfvén waves. These waves are classified as Pi2's as they have an irregular time dependence with periods of 40–150 s.

High-m Alfvén Waves

The magnetic energy stored in the magnetotail that is released in a substorm can also energize the ions on the reconnected flux tubes as they reduce their volume when moving earthward. This results in the injection of energetic ions on dipole-like field lines that will undergo gradient and curvature drifts around the Earth and give rise to the ring current. The addition of these ions to the preexisting plasma produces an unstable particle distribution with free energy that can be converted to Alfvén waves.

The Alfvén waves produced by this mechanism are poloidal, i.e., the magnetic field, plasma displacement and velocity are in a meridional plane. Importantly, their electric field points in the azimuthal direction, as is required to exchange energy with the azimuthally drifting ion population. The resonance condition involves the poloidal Alfvén frequency (which is different to the toroidal frequency), the bounce and drift frequencies of the ions, and the azimuthal wavenumber (m) of the Alfvén wave. For typical values this requires m to be very large (≥ 100). As these high-m Alfvén waves on closed field lines are driven by a resonant interaction, they are also commonly referred to as Field Line Resonances (FLRs).

10.1.3. Other Reviews

For details of studies prior to the remit of this review, readers are referred to Wright and Mann (2006), Keiling (2009), and Keiling and Takahashi (2011). The topics covered by Wright and Mann (2006) are very similar to this review. Keiling (2009) focuses on Alfvén waves in the magetotail. Keiling and Takahashi (2011) discuss the various models of Pi2 excitation and subsequent propagation.

More recently, Nakariakov et al. (2016) have given a comparative review of MHD waves in the Earth's magnetosphere and the solar corona. Hartinger et al. (2022) have reviewed a coordinated effort to consolidate theory and observations of ULF waves in the Earth's magnetosphere. Zong et al. (2017) provide an extensive review of spacecraft observations and test particle simulations of particle flux oscillations associated with standing Alfvén waves in the Earth's magnetosphere. Duan et al. (2022) review the theory and observations of Alfvén waves in the magnetotail associated with substorms. In particular, they focus on the generation of parallel electric fields that arise in kinetic Alfvén waves when finite ion gyroradius effects and finite electron pressure play a role.

10.1.4. Structure of the Review

The remainder of the chapter has the following structure: Section 10.2 summarizes the developments of theoretical ideas and simulations over the last decade that are relevant to terrestrial Alfvén waves; Section 10.3 ties in these ideas with observations of low-m Alfvén waves (those excited by coupling with the fast mode); Section 10.4 focuses on observations of high-m Alfvén waves (driven by resonance with particles); Section 10.5 considers the importance of Alfvén waves for Space Weather; and Section 10.6 gives closing remarks on the wider application of our knowledge of terrestrial Alfvén waves.

10.2. THEORETICAL CONCEPTS AND SIMULATIONS

10.2.1. Global Magnetospheric Simulations

In this subsection, we consider Alfvén waves in global simulations such as the LFM (Lyon et al., 2004) and BATS-R-US codes (Powell et al., 1999). These nonlinear models use the magnetohydrodynamic approximation, and a key feature is that they specify the upstream solar wind conditions. The simulations naturally develop a self-consistent magnetosheath. Magnetic reconnection produces convective motions of magnetospheric flux tubes, including a magnetotail and substorm

behavior. These codes were originally developed to study global magnetospheric structure and the dynamical interaction with the solar wind, rather than Alfvén waves. However, Alfvén waves are a key agent in many magnetospheric processes, such as reconnection and magnetosphere-ionosphere coupling, so it is not surprising that an accurate simulation will provide evidence of Alfvén waves.

Using the LFM code, Claudepierre et al. (2010) specified the upstream solar wind to have monochromatic pressure fluctuations and showed how these could establish toroidal Alfvén waves (Field Line Resonances, FLRs) on dayside closed magnetic field lines where the Alfvén frequency matched that of the driver. This is significant as most of the analytic theories developed at this stage were for axisymmetric equilibria, so these simulations are giving the first evidence that the resonant excitation of Alfvén waves driven by the fast mode will still operate in more general 3D equilibria.

As computer power increased, global simulations were able to adopt more realistic equilibria. A plasmasphere was included in the simulations by Claudepierre et al. (2016), and they found the magnetosphere could respond as a fast waveguide that could drive resonant Alfvén waves both inside and outside the plasmasphere. In particular, the lower Alfvén speed in the plasmasphere allowed the fast mode to penetrate deeper into the magnetosphere and hence facilitated the excitation of plasmaspheric FLRs.

Ellington et al. (2016) used the Space Weather Modeling Framework's (SWMF) code (Tóth et al., 2005) to study the effect of broadband dynamic pressure fluctuations in the solar wind on the magnetosphere. They confirmed the resonant excitation of toroidal Alfvén waves but also observed some local time asymmetries in their amplitudes. They attributed this to various possible causes, such as: coupling to Kelvin-Helmholtz magnetopause surface waves; local time differences in local ionospheric damping rates; and variations in azimuthal wavenumber. This seems reasonable as an increase in ionospheric dissipation will reduce the amplitude of FLRs. Also, it is the magnetic pressure gradient of the fast mode that acts as a driver in the Alfvén wave equation, so we would expect the Alfvén wave amplitude to be dependent on the azimuthal wavenumber. Indeed, Kivelson and Southwood (1986) show that there is an optimum azimuthal wavenumber for drving an FLR; if it is too small, the pressure gradients are also small, and coupling is weak. On the other hand, if it is too large, the fast mode is evanescent, so driving is also weak.

Simulation results for a magnetosphere subject to an impulse in solar wind dynamic pressure were presented by Archer et al. (2022) using the BATS-R-US code. This study focused on the MHD waves excited in response to the impulse. They confirmed field line resonances (FLRs)

were present, and these also exhibited phase mixing. An interesting result of the highly compressed field line geometry around noon is that additional nodes of the magnetic field perturbation can be introduced (that are not present in velocity perturbations), and this can cause a reversal in the handedness of polarization ellipses.

The simulation results presented by Zhang et al. (2012) used solar wind and interplanetary magnetic field data to drive the simulation. They note that reconnection in the magnetotail produces sporadic earthward flows of plasma and is associated with Alfvén waves, particularly where information is communicated to the ionosphere. Yang et al. (2022) also found magnetotail reconnection could produce meridonally narrow flux tubes associated with explosive flows propagating earthward. They note that at the front of these tubes, low Alfvén conductances can be produced. Importantly, the conductance is relatively uniform along the flux tube, and this promotes efficient transport of Alfvénic energy along the tube as reflection from nonuniformity is minimized.

10.2.2. Simulations and Theory of Linear Low-*m* Alfvén Waves

The term 'low-*m*' Alfvén waves (see Section "Low-*m* Alfvén Waves") originates from early studies that used an axisymmetric equilibrium and so could adopt an azimuthal wavenumber *m* to facilitate the analysis. The corresponding Alfvén waves have a toroidal polarization and are driven by the fast mode. The coupling is most efficient for small values of *m* (typically 2–6) as the fast mode becomes evanescent with increasing *m*. Low-*m* Alfvén waves are associated with fast modes in the form of cavity and waveguide modes.

Low-*m* Alfvén waves have a small amplitude (compared to equilibrium quantities), so linear theory can be used. The studies in this subsection have exploited this property to devise simulation codes tailored to study MHD wave behavior rather than the more general magnetospheric dynamics of the global simulation codes of the previous subsection. The linear codes do not have a self-consistent interaction with the solar wind; however, they do resolve wave behavior in the magnetosphere with great clarity and have led to substantial advances over the past decade. An important difference between the global codes and the linear codes is that the latter employ field-aligned coordinates. Indeed, this is the key to achieving clean, high resolutions results, as Alfvén waves can have a small perpendicular scale but a global parallel scale. Field-aligned coordinates allow high resolution in the perpendicular direction without unnecessary (and inefficient) over-resolution in the parallel direction.

Previous studies typically employed an axisymmetric equilibrium, used a simplified magnetic field geometry

and boundaries, and idealized boundary conditions. There is also the distinction between normal mode solutions (where all variables have a prescribed $\exp(i\omega t)$ dependence) and solutions to the time-dependent equations. Progress has been made to generalize all of these details, although individual studies have tended to focus on generalizing one or two aspects.

Ionospheric Boundaries

While field-aligned coordinates are central to the advances described in this subsection, the use of orthogonal field-aligned coordinates has the problem of not fitting a spherical ionospheric boundary. This aspect has been addressed by the introduction of non-orthogonal field-aligned coordinates in several studies (Degeling et al., 2010, 2018; Lysak et al., 2015, 2020; Obana et al., 2015; Takahashi, Lysak, et al., 2018). Studies where the ionospheric boundary is simply taken to be an orthogonal field-aligned coordinate have the property that the Alfvén wave magnetic field is tangential to the ionosphere, so it can easily satisfy a perfectly or partially reflecting boundary condition. For a spherical ionosphere, the Alfvén wave magnetic field is no longer guaranteed to be tangential to the ionosphere, which leads us to question whether FLRs can be excited. A study by Prokopyszyn et al. (2021) shows that FLRs can still be excited, but that an additional evanescent fast mode is present at the ionosphere as a compressional magnetic field perturbation is now required. Hence, the effect on the global FLR is not expected to be significant.

The sunlit ionosphere is generally highly conducting, and many studies adopt the perfectly reflecting limit, which gives a node of the electric field and plasma velocity (Degeling et al., 2010; Wright & Elsden, 2020). When both ionospheres are highly conducting, the standing fundamental Alfvén mode has half a wavelength between ionospheres. When the ionosphere is in darkness, the conductivity can be low, which leads to an antinode of the electric field and plasma velocity. Obana et al. (2015) used a spherical sheet ionosphere to consider an Alfvén wave excited near the terminator such that one footpoint was in a sunlit ionosphere and the other in darkness. They showed how the fundamental standing mode now had a quarter wavelength, as predicted theoretically by Allan and Knox (1979). Such modes have also been found in simulations by Lysak et al. (2020), who adopted a height resolved ionosphere (Lysak et al., 2015). They found that quarter wavelength modes result when the ratio of Pedersen conductances between the sunlit and dark ionospheres is greater than 5.

Outer Boundary and Waveguide/Cavity Modes

The outer boundary for linear models is the magnetopause, as there is no solar wind or magnetosheath.

Often the outer boundary is simply taken as a high latitude dipole field line L-shell (Elsden & Wright, 2017; Lysak et al., 2015; Obana et al., 2015), so these equilibria will not represent waves near the cusp accurately. However, they have proven to be excellent at modeling waves throughout the rest of the magnetosphere. These models have been extended to non-axisymmetric equilibria by allowing for an arbitrary plasma density distribution and adopting a realistic equatorial magnetopause to facilitate studying the flaring of the magnetopause on the flanks and into the tail (Elsden & Wright, 2022; Wright & Elsden, 2020).

The latter used orthogonal coordinates whose coordinate surfaces do not match the outer boundary. Wright and Elsden (2020) show how this can be accommodated by using some suitable interpolation. More complex compressed dipole fields that are non-axisymmetric have been adopted by Degeling et al. (2010, 2018) and, using non-orthogonal coordinates, are able to have a coordinate surface coincide with the magnetopause.

Once the outer boundary has been determined, it is necessary to apply appropriate boundary conditions. Driving by the solar wind is generally regarded as supplying a varying dynamic pressure on the magnetopause, which is modeled by specifying the magnetic pressure on the outer boundary. If the magnetopause is undriven, a node of magnetic pressure is normally applied.

Once the inner and outer boundaries are specified, we can consider fast mode propagation within the system that can carry energy from the magnetopause to locations where resonant coupling to Alfvén waves may take place. For studies that use a closed magnetopause (Degeling et al., 2010, 2018; Lysak et al., 2015, 2020; Obana et al., 2015; Takahashi, Lysak, et al., 2018), cavity modes are relevant. Other studies have mimicked the ability of the magnetotail to let energy flow out into the open tail and leave the system. They do this by introducing a dissipative buffer zone on the nightside such that any waves that enter this region will be dissipated and so will appear to have left the system (Elsden & Wright, 2017, 2019; Wright & Elsden, 2016, 2020).

In an axisymmetric cavity the fast cavity normal modes will simply propagate in the azimuthal direction. When energy is permitted to leave on the nightside, it is appropriate to consider waveguide modes, whose behavior is very different from cavity modes. Elsden and Wright (2019) used a line dipole equilibrium and found that the non-axisymmetric waveguide normal mode had a spatially standing nature in azimuth around noon, which switched to anti-sunward propagation on the flanks. They found this behavior persisted in an analytical cartesian model, including the property that these modes decay in time as they lose energy to the tail. Using an equilibrium based on a 3D dipole with flaring magnetopause on the flanks Wright and Elsden (2020) found these

properties persisted even when an axisymmetric density was assumed.

Driver Properties

The models in this subsection represent solar wind driving by applying a time-dependent pressure on the outer boundary (the magnetopause). Some simulations have focused on strictly monochromatic solutions and reported normal mode properties (Degeling et al., 2018; Wright & Elsden, 2016; Wright et al., 2022). Others have considered a steady monochromatic driver to focus on the time dependent evolution to a normal mode (Elsden & Wright, 2017). This study demonstrated how phase mixing persists in 3D resonant coupling and confirmed the formula for the width of the resonance as a function of time (derived in 1D by Mann et al. (1995)) remains accurate in 3D. It also validates formulae for the saturated width and amplitude of the resonance against simulation results. Lysak et al. (2015) and Degeling et al. (2010) used a decaying monochromatic driver, while others have used a broadband impulse of pressure (Elsden & Wright, 2018, 2019, 2022; Takahashi et al., 2016; Wright et al., 2018; Wright & Elsden, 2020). All these studies show clear evidence of resonant Alfvén waves, either at the driver frequency (for monochromatic driving) or the waveguide/cavity frequencies (for impulsive driving).

It is also important to consider where the driving pressure is applied. Some studies focus on the nightside outer boundary to represent the effect of substorms in the magnetotail releasing energy earthward and causing wave behavior similar to Pi2's (Lysak et al., 2015). Other studies have focused on dayside or flank driving (Degeling et al., 2010, 2018; Elsden & Wright, 2017, 2019; Wright & Elsden, 2016, 2020; Wright et al., 2018, 2022). These studies have shown the importance of the location of the energy source on the locations where FLRs are established. When the magnetopause is driven on the nightside, Alfvén resonances tend to be excited there (Lysak et al., 2015). Both Degeling and Rankin (2008) and Elsden and Wright (2019) show how varying the local time of the driver from noon toward dusk excites Alfvén waves more on the dusk flank. This raises the possibility of using the location of Alfvén waves to constrain where energy crosses the magnetopause.

Local Time Dependence and Plumes

If the equilibrium and driver are symmetric about noon, the resonant Alfvén waves that are excited are also symmetric. Elsden and Wright (2018) show how the location of the Alfvén waves is relatively insensitive to the spatial and temporal scale of the driver so long as the waveguide modes, are excited. This is because it is the pressure gradients of the fast waveguide modes that actually drive the FLRs.

In reality, the magnetosphere is not symmetric about noon as the dusk flank is more dense and has lower Alfvén frequencies than at dawn. Observations show that Alfvén waves are more frequently excited, and with greater amplitude, at dawn rather than dusk (Takahashi et al., 2015). It seems plausible that this may be due to the Kelvin-Helmholz instability operating more effectively at dawn, however, Takahashi et al. (2016) show this is not the case. They also present simulations which explain the dawn/dusk Alfvén wave asymmetry in terms of the dependence of the efficiency of fast and Alfvén wave coupling on the density gradient. Wright et al. (2018) also explored the dawn/dusk asymmetry in a magnetosphere with an asymmetric density and Alfvén speed variation. Even when they applied a symmetric pressure pulse to the magnetopause, the asymmetric refraction of the fast mode was seen to excite larger amplitude Alfvén waves at dawn compared to dusk. This is consistent with other studies (Archer et al., 2015, 2017) that found fast cavity and waveguide modes may be more frequent at dawn compared to dusk due to the different local wave speed profiles.

Following substorms, there are occasions when a plasma drainage plume allows plasmaspheric material to extend into the magnetosphere beyond the nominal plasmapause (Lambour et al., 1997). This can give rise to rapid variations of density with magnetic local time (MLT) in the afternoon sector. Numerical studies of Alfvén wave FLRs with a plume present have been completed as both normal mode (Degeling et al., 2018) and impulsively driven (Wright & Elsden, 2020) calculations. Figure 10.3 is taken from the latter study and shows the depression in Alfvén speed (in the equatorial plane) associated with a dense plasma plume in the afternoon. The Alfvén speed outside the plume is axisymmetric.

Figure 10.3(b) uses $j_\parallel$ to identify where the Alfvén waves are. Several interesting features are evident in this figure. The nested colored ridges are actually contours of the Alfvén wave frequency (figure 8(b) of Elsden and Wright (2017) and figure 4 of Elsden and Wright (2018)). On the dawnside ($y < 0$), the equilibrium is locally axisymmetric, so 2D theory applies here and, as expected (Wright & Thompson, 1994), Alfvén waves sit on circles of constant L (see the reference dashed circles in panel (b)). As we move radially outward the Alfvén frequency decreases giving rise to phase mixing, which manifests as successive colored ridges.

The situation is quite different in the afternoon. Tracing a ridge from noon, it moves inward and crosses L-shells on encountering the plume and then moves back out to larger L-shells on leaving the plume. The Alfvén wave current ridges in 2D theory (applicable at dawn, $y < 0$) sit on circles, but on the edges of a plume they
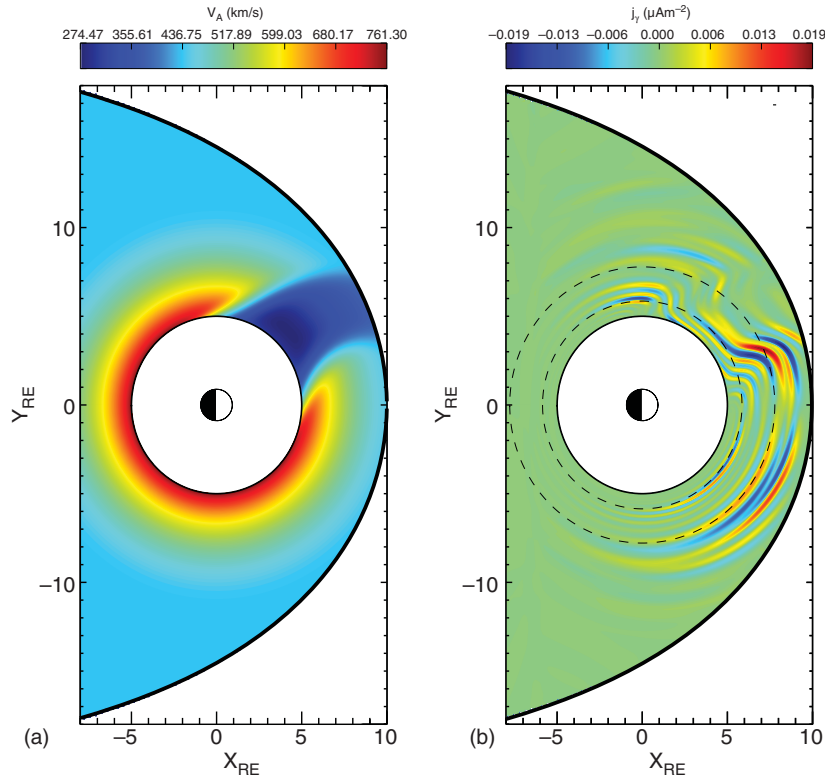
Figure 10.3 Simulation results (Wright & Allan (2020) /John Wiley & Sons). (a) The Alfvén speed in the equatorial plane with a plasma drainage plume in the afternoon. (b) The Alfvén wave currents resulting from an impulsive pressure pulse. (The field-aligned current is calculated at the ionospheric end and then mapped along the field line and plotted in the equatorial plane.)
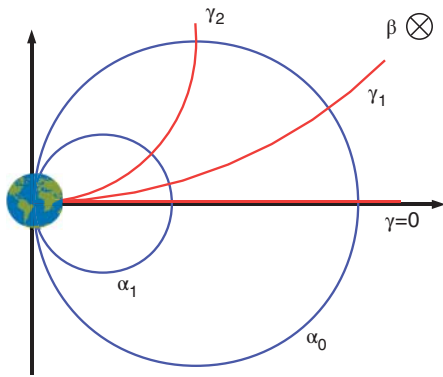
Figure 10.4 The orthogonal field-aligned coordinates (α, β, γ) for a dipole field (Wright & Allan (2016) / IOP Publishing).

can be inclined. Indeed, the ridges at $(x, y) = (4.5, 6.5)$ are almost perpendicular to L-shells. On the edges of a plume the equilibrium is far from 2D because of the rapid variation in density with azimuth, yet resonant Alfvén waves are clearly present (Degeling et al., 2018; Wright & Elsden, 2020). These locations are ideal for studying the differences between 2D and 3D FLRs,

and virtual satellite observations have been generated by Elsden and Wright (2022), which show substantial differences from 2D toroidal FLRs. The principal difference being that in 2D (axisymmetric models) the Alfvén wave velocity and field perturbations are in the azimuthal direction, while on the edges of a plume they have a polarization somewhere between poloidal and toroidal.

Alfvén Wave Polarization and Resonance Maps

Before considering Alfvén waves of arbitrary polarization, we study their properties in the toroidal and poloidal limits using field-aligned coordinates (α, β, γ), as shown in Figure 10.4. In 2D (line dipole) and 3D dipole equilibrium magnetic fields the coordinate directions are orthogonal, with surfaces of constant α corresponding to nested axisymmetric surfaces of field lines (the L-shells defined in Section "Low-m Alfvén Waves"). The invariant azimuthal coordinate is β. Along a given field line α and β have constant values, so they can be used to label the field lines. The position along a field line is specified by the γ coordinate.

The equations for the poloidal and toroidal Alfvén frequencies are given in Wright and Elsden (2016) as

$$\frac{\partial}{\partial \gamma}\left(\frac{1}{h_\gamma}\frac{\partial U_\alpha}{\partial \gamma}\right) + \frac{1}{h_\gamma}\frac{\partial}{\partial \gamma}\left(\ln\left(\frac{h_\alpha}{h_\beta}\right)\right)\frac{\partial U_\alpha}{\partial \gamma} + \frac{\omega_A^2}{V_A^2}h_\gamma U_\alpha = 0,$$

(10.2)

$$\frac{\partial}{\partial \gamma}\left(\frac{1}{h_\gamma}\frac{\partial U_\beta}{\partial \gamma}\right) + \frac{1}{h_\gamma}\frac{\partial}{\partial \gamma}\left(\ln\left(\frac{h_\beta}{h_\alpha}\right)\right)\frac{\partial U_\beta}{\partial \gamma} + \frac{\omega_A^2}{V_A^2}h_\gamma U_\beta = 0.$$

(10.3)

The quantities h_α, h_β, and h_γ are in general functions of (α, β, γ) and are scale factors that encapsulate the magnetic field geometry and strength (B). U_α and U_β are simulation variables that are related to the transverse velocity components (u_α and u_β) by $U_\alpha = u_\alpha h_\beta B$ and $U_\beta = u_\beta h_\alpha B$. The Alfvén speed is V_A, and the Alfvén frequency is ω_A.

Equation (10.2) has plasma displacement and velocity in the α (poloidal) direction, so the frequency corresponds to the poloidal Alfvén wave frequency. In Equation (10.3) the wave has a toroidal polarization (aligned with β), so ω_A here corresponds to the toroidal Alfvén frequency. The middle term of these equations shows that if h_α/h_β varies along the field line, then the toroidal and poloidal frequencies will be different.
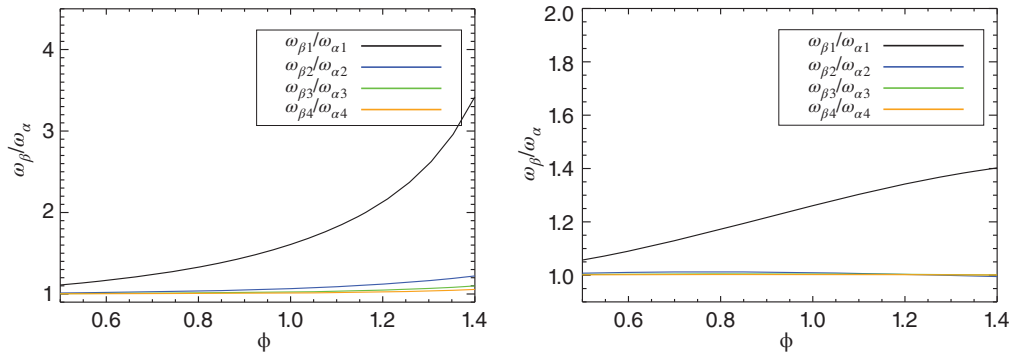
Figure 10.5 shows the ratio of toroidal frequency (ω_β) to poloidal frequency (ω_α) as a function of invariant latitude (the latitude of the field line footpoint in the ionosphere). The invariant latitude range shown of 0.5 to 1.4 rad corresponds to $\sim 28°$ to $\sim 80°$. The left-hand panel used a 2D line dipole, and the right-hand panel used a 3D dipole. (A 2D line dipole field is the magnetic field surrounding a pair of infinitely long straight wires that carry an equal, but opposite, current. If the wires are aligned with the y direction, the magnetic field will be invariant in this direction, and only the x and z components of the field will be nonzero.) The black lines show the frequency ratios for the fundamental toroidal and poloidal modes which clearly have the greatest difference. Even for a modest invariant latitude of 60° (~ 1 rad) the line dipole has $\omega_\beta/\omega_\alpha \approx 1.6$,

which is much greater than that of the 3D dipole where the ratio is 1.25. This led Wright and Elsden (2016) to adopt the line dipole field as the discrepancy between toroidal and poloidal Alfvén frequencies is substantial and makes it easy to see the features of 3D Alfvén resonances very clearly with modest computing power.

Returning to Figure 10.3(b), we know that the Alfvén waves in the pre-noon sector at $(x, y) = (7, -5)$ exist in an equilibrium that is locally independent of azimuth, so have a plasma velocity aligned with the azimuthal direction. However, the direction of the plasma velocity on the edges of the plume (where the Alfvén wave ridges cross L-shells as the equilibrium is 3D here) is not so obvious. This property was addressed by Wright and Elsden (2016) in a normal mode calculation from which Figure 10.6 is taken. The figure shows a close-up view in the equatorial plane where the resonant Alfvén wave ridge is inclined to the azimuthal direction by around 35°. The color contours show time-averaged energy density. As the resonant Alfvén wave amplitude is much greater than the fast mode, this is a good proxy for the location of the Alfvén wave. The vectors show the direction of the plasma velocity, which is evidently aligned with the path of the resonant ridge.

Resonant Alfvén waves in 3D require us to go beyond the current ideas of poloidal and toroidal Alfvén waves and to consider waves with an arbitrary polarization. To determine the Alfvén frequency for such waves on a particular field line, Wright and Elsden (2016) considered the local α and β directions in the equatorial plane for this field line. These directions are then rotated by an angle θ to produce new coordinate directions, called α' and β'. Naively, we might expect the corresponding Alfvén wave equation to be

$$\frac{\partial}{\partial \gamma}\left(\frac{1}{h_\gamma}\frac{\partial U_{\beta'}}{\partial \gamma}\right) + \frac{1}{h_\gamma}\frac{\partial}{\partial \gamma}\left(\ln\left(\frac{h_{\beta'}}{h_{\alpha'}}\right)\right)\frac{\partial U_{\beta'}}{\partial \gamma} + \frac{\omega_A^2}{V_A^2}h_\gamma U_{\beta'} = 0,$$

(10.4)

Figure 10.5 Ratio of the toroidal (ω_β) to poloidal (ω_α) Alfvén frequencies for a line dipole (left) and a 3D dipole (right) as a function of invariant latitude over the range 0.5 to 1.4 rad (28° to 80°). Black, blue, green, and brown correspond to the first four harmonics. Source: Reproduced from Elsden (2016) / University of St Andrews Library.
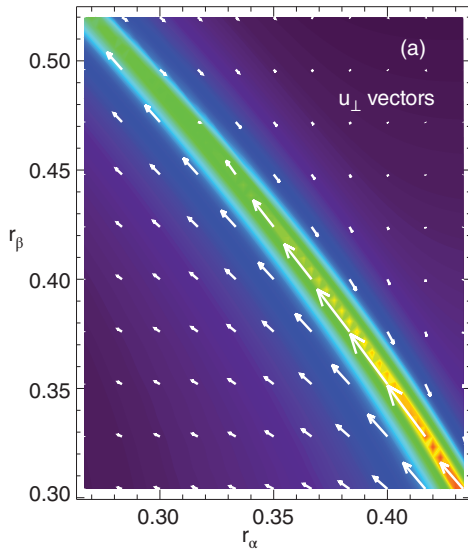
Figure 10.6 A close-up view in the equatorial plane of time-averaged energy density, which is indicative of the location of the resonant Alfvén waves. The arrows show the plasma velocity, which is aligned with the path of the resonant Alfvén waves. Source: Reproduced from Elsden (2016) / University of St Andrews Library.

where $h_{\alpha'}$ and $h_{\beta'}$ are the scale factors for the rotated coordinate system. There are some issues with the existence of orthogonal coordinates for the rotated system (Salat & Tataronis, 2000). Nevertheless, Wright and Elsden (2016) show how the effective scale factors can be calculated for Equation (10.4) to be applicable. They provided analytical expressions for the scale factors. In more general fields, the scale factors can be calculated by tracing neighboring field lines and considering their separation (Degeling et al., 2010, 2018; Wright et al., 2022).

The result of solving Equation (10.4) is to determine the Alfvén frequency for a given polarization angle, $\omega_A(\theta)$,

and such results are shown in Figure 10.7(a). The range of θ is 0 to $\pi/2$, corresponding to toroidal and poloidal polarizations, respectively. The values of ω_A in these two limits are identical to the solutions of Equations (10.3) and (10.2), so these are familiar results. What is not so well known is that ω_A can change smoothly and continuously between these two values, as shown by the $\omega_A(\theta)$ curves.

Recalling that α and β have constant values on a given field line, we see that Figure 10.7(b) has five red dots that label five different field lines. (For the scale factors used in Figure 10.7, α and β are equivalent to radial and azimuthal distances in the equatorial plane.) For field line (e), $\omega_A(\theta)$ is given by the top line in the left-hand panel. If the normal mode is driven with a frequency ω_d (indicated by the horizontal line in Figure 10.7(a)), then it is not possible to choose a polarization for this field line such that $\omega_A(\theta) = \omega_d$, so this field line is termed 'non-resonant.'

Assuming a simple radial monotonic variation in Alfvén speed, we can move radially out (in α) to get to the field line (a). Curve (a) in Figure 10.7(a) shows that this field line can meet the resonant condition $\omega_A(\theta) = \omega_d$ if we choose the polarization angle to be $\theta = \pi/2$, which is the poloidal direction and is indicated by the short black line attached to the red dot labeled (a). Proceeding radially outward to field line (c), we need to choose an angle $\theta = \theta_c$ (which is intermediate to the toroidal and poloidal directions) to match the resonant condition. Moving radially further out to field line (b), we are just able to match the resonance condition with a toroidal ($\theta = 0$) polarization, but field lines beyond this will be non-resonant. This procedure can be repeated for different azimuths (β) to identify the Resonant Zone (where a resonant polarization exists) and Non-Resonant Zones (where a resonant polarization does not exist). The regions are separated by Resonant Zone Boundaries where resonance requires a
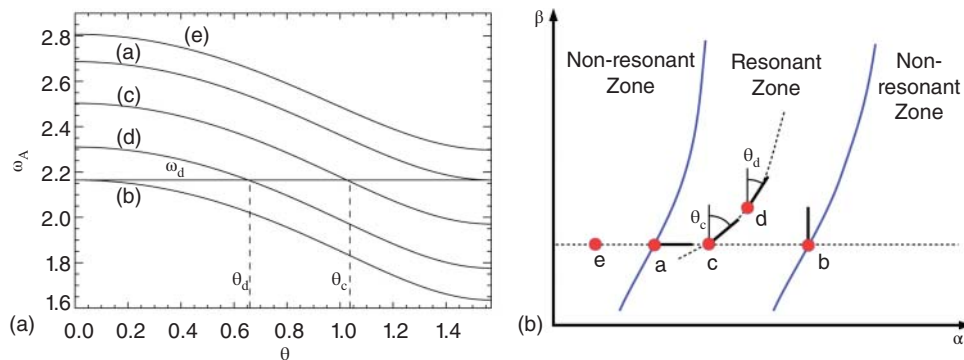
Figure 10.7 (a) The variation of Alfvén frequency, ω_A, with polarization angle, θ, for five different field lines. Toroidal and poloidal polarizations correspond to $\theta = 0$ and $\pi/2$, respectively. The horizontal line denotes the driving frequency, ω_d. (b) The Resonance Map showing the locations of the five field lines along with their resonant polarizations such that $\omega_A(\theta) = \omega_d$. Source: Reproduced from Elsden (2016) / University of St Andrews Library.

toroidal or poloidal polarization. Figure 10.7(b) is known as a Resonance Map (Wright & Elsden, 2016).

Wright and Elsden (2016) show how these ideas may be combined to deduce an equation for the path the resonant ridge takes in Figure 10.6 as **u** is aligned with this ridge. Consider again field line (c) in Figure 10.7(b): we require the plasma velocity to be aligned with the short black line with an angle θ_c for this field line to be resonant. Hence, the resonant Alfvén wave ridge will coincide with this line (as shown in Figure 10.6). Stepping incrementally in this direction to field line (d), which will also be on the ridge, we need to adopt a polarization angle θ_d (which is slightly different from θ_c) to be resonant. Proceeding in this fashion, the entire path of the resonance can be mapped out in 3D and is denoted by the curved dashed line.

Figure 10.7(a) was constructed for a line dipole. The symmetry of this field leads to the $\omega_A(\theta)$ curves being symmetric about $\theta = \pi/2$. Thus, besides field line (c) being resonant for polarization angle $\theta = \theta_c$, it will also be resonant for $\theta = \pi - \theta_c$, so we could introduce a second resonant path in panel (b) through field line (c) that is inclined at this angle. It is also a property of the line dipole (and the 3D dipole) that the maximum ω_A is always the toroidal frequency and the minimum is always the poloidal. This is not true for more general fields such as the compressed dipole field considered by Degeling et al. (2010) and Wright et al. (2022), from which Figure 10.8 is taken.

One generalization evident in a compressed dipole field is that the maximum and minimum ω_A on a field line no longer correspond to the toroidal and poloidal directions. The Resonant Zone Boundaries are now identified as where the maximum and minimum ω_A match ω_d. Figure 10.8(a) shows these boundaries as red lines, between which is the Resonant Zone. For an MLT of 0 hours (midnight, $(x, y) = (-9, 0)$) the resonant paths (black lines) approach the outer boundary with a toroidal polarization (i.e., $\omega_A(\theta_r) = \omega_d$ if $\theta_r = 0$). In contrast, the resonant paths approach the same outer boundary at noon (12 MLT, $(x, y) = (9, 0)$) with a poloidal orientation ($\theta_r = 90°$). Indeed, θ_r on the outer boundary changes continuously with MLT on both boundaries, as summarized in Figure 10.8(b). We note that at noon the poloidal frequency is greater than the toroidal, which is the opposite of the situation for an uncompressed dipole. This is due to the field lines in a meridional plane not having monotonic convergence between the equator and ionosphere and is the same geometric property that led to the unusual hodogram polarization changes reported by Archer et al. (2022) and discussed in subsection 10.2.1.

The family of resonant paths shown in Figure 10.8(a) are selected paths from an infinite number of possible solutions as every point in the Resonant Zone could potentially lie on the resonant Alfvén wave ridge.

Simulation results (Degeling et al., 2010, 2018; Wright & Elsden, 2016; Wright et al., 2022) show that only one or two of these paths describe where the resonant Alfvén waves are actually found in a given simulation. Figure 10.8(c) is a simulation result with a Resonance Map like that in panel (a). The color contours are of field-aligned vorticity magnitude in the equatorial plane. Overplotted are black lines showing the possible resonance paths. Clearly, one particular path coincides with the resonant ridge, and this is shown as the green and black dashed line in panel (a). This particular resonant path seems to be favored as it corresponds to a separatrix of the resonant paths that Mager and Klimushkin (2021) explain is special as Alfvén wave energy will naturally accumulate there. Wright et al. (2022) also note that this particular resonant path is special as it meets the Resonant Zone Boundaries with a tangential alignment. This condition also applies in situations where there is only one Resonant Zone Boundary, meaning a separatrix cannot be defined (see figure 5 of Wright et al. (2022)). The examples of Resonance Maps considered so far have Resonant Zones that do not encounter the boundaries of the simulation domain (excluding periodic boundaries). When simulation boundaries are encountered, the boundary conditions there can be used to identify the resonant path that coincides with the simulation results (Wright & Elsden, 2016).

An alternative formulation of the governing equations (assuming $b_\parallel = 0$) by Degeling et al. (2010) yielded an eigenvalue problem for two Alfvén wave eigenmodes. Interestingly, these coincide with the Resonant Zone Boundaries as defined by Wright and Elsden (2016). This suggests the possibility that Degeling's eigenvalue calculation may be an efficient method of finding the Resonant Zone Boundaries, in contrast to the method of Wright and Elsden (2016), which requires iterating the shooting method to solve equation (10.4) and further iteration to determine the position where Max/Min$[\omega_A(\alpha, \beta)] = \omega_d$. It is yet to be shown mathematically that these two approaches are equivalent (Elsden et al., 2022).

Recently, Mager and Klimushkin (2021) derived analytical normal solutions in the high-m limit, which means the fast mode may be neglected as it is evanescent so may not provide an effective driver of the resonant Alfvén waves (Elsden et al., 2022). They produced an analytical formula for the 3D Alfvén wave equation, which should be equivalent to Equation (10.4). Extrapolating 1D and 2D results to 3D would suggest that at the resonance $u_{\beta'}$ would have a $1/\alpha'$ singularity and $u_{\alpha'}$ would have a logarithmic singularity. Mager and Klimushkin (2021) found the logarithmic singularity was absent and that $u_{\alpha'}$ remained finite, but with small-scale oscillations in α'. It would be interesting to look for these properties in the simulations results.
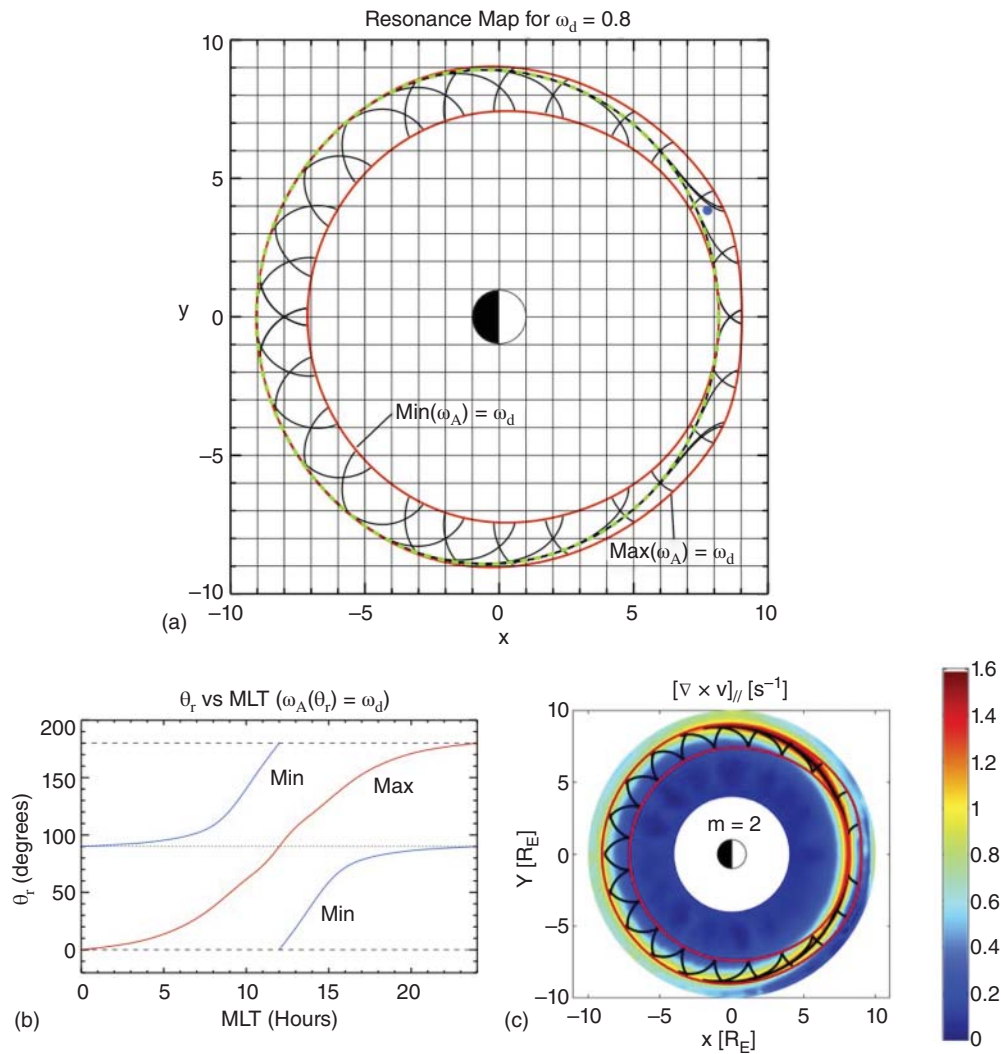
Figure 10.8 (a) Resonance Map in the equatorial plane for the compressed dipole equilibrium used in Wright et al. (2022). The Resonant Zone Boundaries are shown in red. Black lines indicate permissible resonant Alfvén wave paths. (b) The variation of the resonant polarization angle (θ_r) on the boundaries of the Resonant Zone with magnetic local time. (c) Alfvén wave amplitude (using parallel vorticity) in the equatorial plane with the resonant paths from (a) overplotted. The resonant ridge coincides with one particular path that is shown as the dashed black and green line in (a).

The approach used by Mager and Klimushkin (2021) to construct resonant paths is to consider the perpendicular group velocity of the Alfvén waves to work out the direction the wave will propagate perpendicular to the field, as this will be tangential to the paths. The Resonant Zone Boundaries are found by equating the toroidal or poloidal frequency with the normal mode frequency (ω_d) in their axisymmetric magnetic field equilibrium.

Recently, Elsden et al. (2022) have provided a detailed review of the theory of 3D Alfvén resonances research and Resonance Maps. They cover both analytical work and computational studies. The review is a useful resource for readers who would like a more detailed account than given here.

10.2.3. Modeling High-*m* Poloidal Waves

This section concerns recent modeling of high-m poloidal waves in theory and simulation. Observations of high-m waves are reserved for Section 10.4. As briefly discussed in Section "High-*m* Alfvén Waves", high-m Alfvén waves are generally internally driven by resonance with particle populations with the appropriate drift and bounce frequencies (Southwood et al.,

1969) (the resonance condition is further discussed in Section 10.4).

Once established, Radoski (1974) first predicted, from consideration of the undriven poloidal/toroidal Alfvén wave equations in a cylindrical geometry, that the poloidal mode will decay over time. This was put on a firmer theoretical footing by Mann and Wright (1995), who showed numerically in a Cartesian box model that there is a polarization rotation in time from poloidal to toroidal. This transition is governed by phase mixing (Heyvaerts & Priest, 1983), which acts to reduce the wavelength in the direction of varying Alfvén frequency (usually the radial direction). In the case studied by Mann and Wright (1995), however, due to the straight magnetic field, the poloidal and toroidal Alfvén frequencies of any one field line are the same. Hence, this polarization rotation occurs on a single field line.

Considering the ideas developed in the preceding sections (in a dipole field) the poloidal/toroidal fundamental Alfvén frequencies differ substantially (see Figure 10.5). Therefore, a simple rotation from one to the other at a fixed location, maintaining the same frequency, is no longer viable. This idea led Elsden and Wright (2020) to consider the evolution of an initially poloidal Alfvén wave in a 2-D dipole magnetic field. Using a similar numerical model to that described in Section 10.2.2 (e.g., Wright & Elsden, 2020), a dominantly poloidal mode was initialized. The top panels of Figure 10.9 show contour plots of the initial (a) radial and (b) azimuthal velocity (proportional to azimuthal and radial electric fields, respectively). The plots are made in the equatorial plane, with α and β representing the radial and azimuthal directions, respectively. Panels (c)–(f) show the evolution of the wave fields in time by plotting the magnitude of the perpendicular velocity. Phase mixing is apparent after a few wave periods (the period is $\tau = 1.342$ in dimensionless units), reducing the local radial wavelength in (c). Over time in panels (d)–(f), the region of maximum amplitude appears to travel away from the initialized region shown in (a) along well-defined curves.

It was shown that these curves are in fact contours of Alfvén frequency, as proved by the white lines overlaid in panel (g). These lines represent solutions to Equation (10.4), using a driving frequency corresponding to the poloidal Alfvén frequency at a particular location along $\beta = 0$, where the wave is initialized. These lines are therefore the Resonant Zone paths described in Section "Alfvén Wave Polarization and Resonance Maps". The perturbations travel along these paths, continuously rotating polarization from poloidal to toroidal (the wave polarization at any point is tangential to the local Alfvén frequency contour). This type of behavior had been first considered analytically in a normal mode formulation by Leonovich and Mazur (1993) and Klimushkin

et al. (1995). The numerical results in Figure 10.9 give conclusive proof that this, perhaps counter-intuitive behavior, is possible: if Alfvén waves are incompressible and have a Poynting vector and group velocity strictly aligned with the equilibrium field, how can they travel perpendicular to this direction? A careful analysis of the simulation fields allowed Elsden and Wright (2022) to answer this conundrum. Leonovich et al. (2015) showed how these ideas can be used to explain the polarization features in the poloidal Alfvén wave observations reported by Dai et al. (2013), which are discussed further in Section 10.4.

In Figure 10.9, it should be stressed that the behavior of the peak wave amplitude traveling along contours of Alfvén frequency is far more pronounced for the fundamental (panel (g)) than for the second harmonic (panel (h)), due to the increased difference between the poloidal and toroidal frequencies for the fundamental (e.g., Figure 10.5).

To more realistically model waves driven by azimuthally drifting particles (drifting by gradient and curvature drifts), azimuthal phase motion has to be taken into account. Figure 10.10 is a reproduction of figure 10 from Elsden and Wright (2020), showing results from a simulation where such azimuthal phase motion is included, as well as multiple wavelengths in azimuth to genuinely model the 'high-m' regime. The figure displays the magnitude of the perpendicular velocity in the equatorial plane at four different times in the simulation, with the simulation configuration at $t = 0$ in panel (a) showing the initially dominant poloidal wave. Over time, phase mixing reduces the local wavelength in α. The plasma velocity is aligned with the colored ridges, so it is poloidal at $t = 0$ and rotates toward toroidal as time increases. The inclination of the ridges, being aligned with the plasma velocity, can also be thought of as the polarization angle of the Alfvén waves introduced in Section "Alfvén Wave Polarization and Resonance Maps". Elsden and Wright (2020) show how the orientation of these fronts can be determined by considering how the waves will phasemix through the dependence of the Alfvén frequency on the polarization (θ) and radial location (α), such that $\omega_A = \omega_A(\alpha, \theta)$ (the medium is independent of azimuth β). Using the fact that the wave phase is constant along the phase fronts, it can be shown that these fronts must satisfy

$$\frac{d\beta}{d\alpha} = \frac{k_\alpha}{k_\beta} = -\left(\left.\frac{\partial \omega_A}{\partial \alpha}\right|_\theta + \left.\frac{\partial \omega_A}{\partial \theta}\right|_\alpha \left.\frac{\partial \theta}{\partial \alpha}\right|_t \right) \frac{t}{k_\beta}, \qquad (10.5)$$

for azimuthal wavenumber k_β (and local radial wavenumber k_α), with the wave polarization defined by

$$\theta = \tan^{-1}\left(\frac{d\alpha}{d\beta}\right). \qquad (10.6)$$
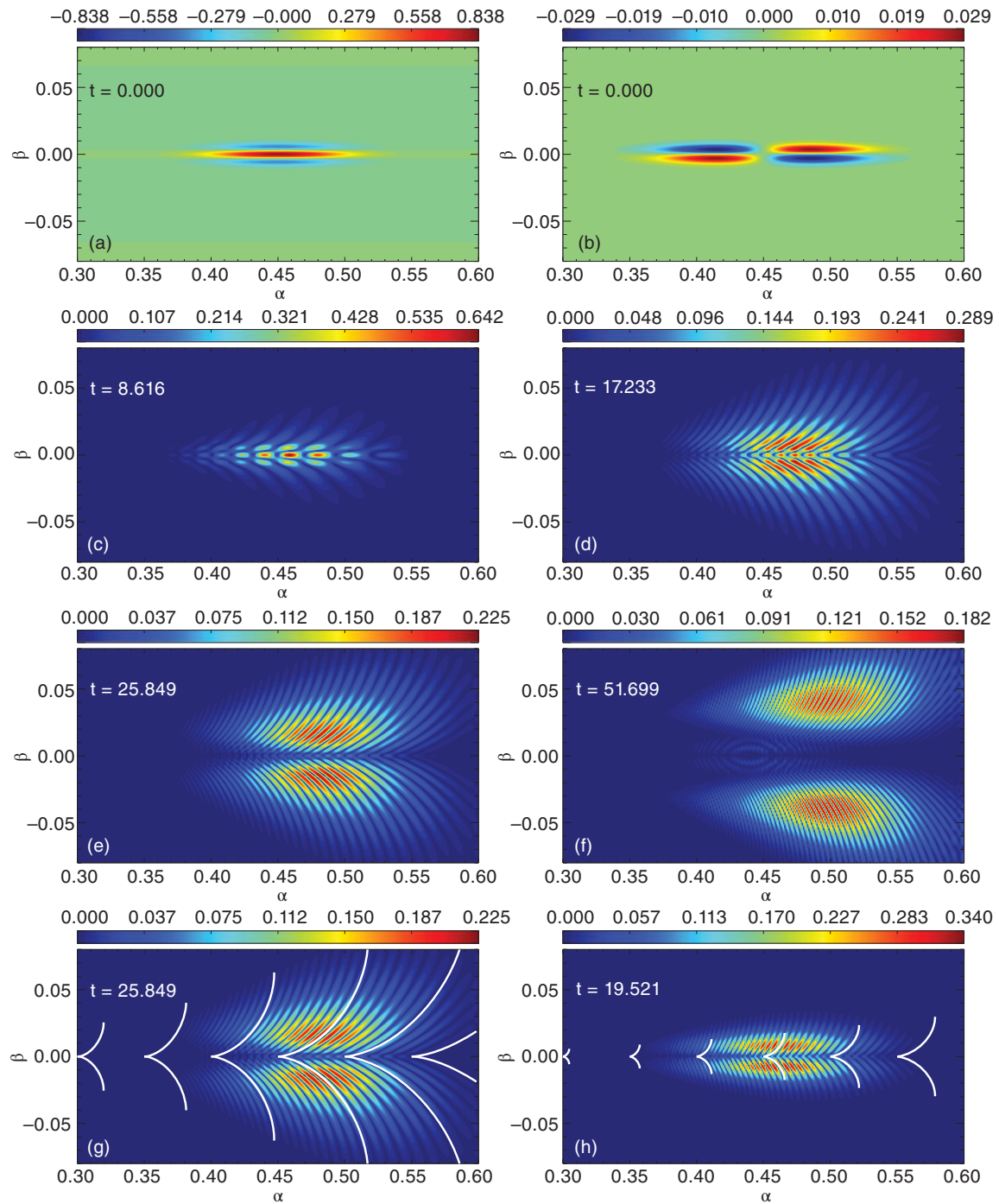
Figure 10.9 Reproduction of figure 1 from Elsden & Wright (2020) showing the evolution of a poloidal Alfvén wave in a dipole magnetic field. α and β are the radial and azimuthal directions, respectively. In the equatorial plane: initial condition for (a) radial velocity, (b) azimuthal velocity; (c)–(f) magnitude of perpendicular velocity at four different simulation times; (g) same as panel (e) with contours of Alfvén frequency overlaid in white for the fundamental mode; (h) Color contour of $|B_\perp|$ from a separate simulation for the second field-aligned harmonic, with overlaid Alfvén frequency contours in white.
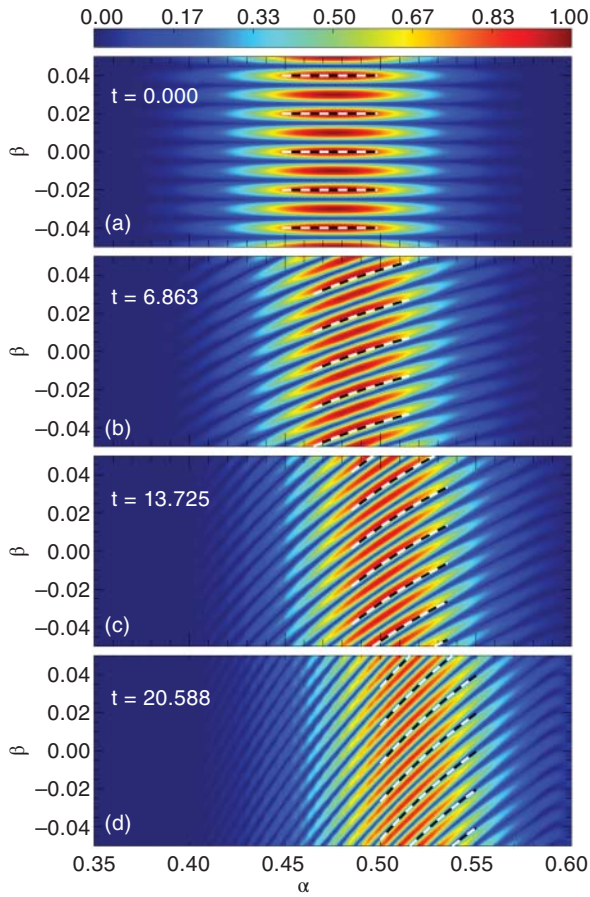
Figure 10.10 Source: Reproduction of figure 10 by Elsden and Wright (2020). Plotted are contours of the magnitude of the perpendicular simulation velocity $|U_\perp|$ in the equatorial plane for a simulation with multiple azimuthal wavelengths together with azimuthal phase propagation at increasing times (a)–(d). Fits to the phase fronts are overplotted as dashed lines and are further described in the main text.

Equation (10.5) describes how the gradient of the phase fronts in the equatorial (α, β) plane changes in time and can be used to trace the dashed black and white lines overlaid in Figure 10.10, which clearly match well to the velocity contours. Several interesting features are evident in Equation (10.5). It is a generalization of the simpler axisymmetric toroidal phase mixing picture, which has a phase-mixing length across L-shells of $L_{ph} = 2\pi/(td\omega_{AT}/dL)$ for local toroidal Alfvén frequency ω_{AT}. Since $L \equiv \alpha$ here, this corresponds to the local wavelength in α, giving $k_\alpha = td\omega_{AT}/d\alpha$. Note that as $k_\beta = 0$ for axisymmetric Alfvén waves, they will remain toroidally polarized and oscillate with frequency ω_{AT}. The phase fronts are inclined at an angle $\tan^{-1}(k_\beta/k_\alpha) = 0$ to the toroidal direction. Equation (10.5) shows how this generalizes for phase mixing Alfvén waves when $k_\beta \neq 0$ and the polarization angle of the waves can change in

time. The dependence $k_\alpha \propto t$ is still evident; however, it is no longer simply multiplied by $d\omega_{AT}/d\alpha$, but by

$$\left.\frac{\partial\omega_A(\alpha,\theta)}{\partial\alpha}\right|_\theta + \left.\frac{\partial\omega_A(\alpha,\theta)}{\partial\theta}\right|_\alpha \left.\frac{\partial\theta}{\partial\alpha}\right|_t. \qquad (10.7)$$

This can be used to recover the toroidal case by noting $\partial\theta/\partial\alpha = 0$ and $\omega_A(\alpha,\theta) = \omega_{AT}$ as $\theta(\alpha) = 0$ in this limit. The more general expression accounts for the fact that as the waves phasemix, their polarization changes, which means the waves need to move to different field lines to maintain their original frequency. This migration is evident in Figure 10.10, as the waves begin centered on $\alpha = 0.475$ and end up centered on $\alpha = 0.52$.

There have been several other recent modeling efforts to better understand high-m Alfvén waves in the magnetosphere. Choi and Lee (2021) considered a high-m mode in an axisymmetric dipole to provide an explanation as to how poloidal modes could be very long lasting even in the absence of a clear driving energy source. They showed that in regions where the Alfvén speed is locally not varying in the radial direction (e.g., Denton et al., 2003; Le et al., 2017), such poloidal modes can last for several periods. This is simply due to phase mixing, which depends critically on the Alfvén frequency gradient, occurring more slowly, as is evident from setting $\partial\omega_A/\partial\alpha|_\theta = 0$ in Equation (10.5).

In a series of three papers, Yamakawa et al. (2019, 2020, 2022) investigate ring current ions driving poloidal ULF waves using the drift-kinetic simulation GEMSIS-RC (Geospace Environment Modeling System for Integrated Studies-Ring Current). The model also solves Maxwell's equations, providing the required ULF wave fields. Across the three studies, it is clearly demonstrated that ring current ions drive poloidal ULF waves by both drift and bounce resonance in the Pc3-5 frequency band. A key requirement for this is found to be a positive energy gradient in the ion phase space density (PSD).

10.2.4. Auroral Particle Acceleration by Alfvén Waves

It is evident that Alfvén waves can be established on terrestrial field lines through a variety of processes. Specifically, the fast mode can excite Alfvén waves on closed dipole-like field lines (Section 10.2.2) and on stretched field lines in the magnetotail (Section "Magnetotail and Nightside Alfvén Waves"). Alfvén waves can also be produced from reconnection and high-m Alfvén waves from wave particle interactions (Southwood et al., 1969). Whatever the origin of these Alfvén waves, they all possess field-aligned currents that are carried predominantly by electrons moving along magnetic field lines. As the currents flow toward the ionosphere, they are intensified considerably by the narrowing

of the flux carrying the Alfvén wave, whose cross-sectional area scales as $1/B$. Strong currents require a large flux of electrons along the flux tube and necessitate an acceleration region at altitudes of 1-2 R_e (see Figure 10.2 and Section "Magnetotail and Nightside Alfvén Waves"). The currents are so strong that the electron energy flux deposited in the ionosphere can produce a visible aurora. A proper consideration of electron energization requires a two-fluid or kinetic formulation. However, single-fluid MHD models can be used to predict likely auroral signatures using the strength of the field-aligned current as a proxy for electron kinetic energy flux.

Wright and Allan (2008) applied this approach to nightside PSBL field lines. They found that larger amplitude Alfvén waves were excited on the PSBL field lines compared to those in the tail lobe. Moreover, the strong Alfvén speed gradient across the PSBL leads to large field-aligned currents. Working with a cartesian simulation geometry and scaling to ionospheric altitudes, they could produce realistic temporal and spatial scales for auroral arcs. These features move with the Alfvén wave phase velocity in an equatorward direction, which is determined by the direction of the Alfvén speed gradient across the PSBL.

Alfvén waves on closed dipole-like field lines can also be associated with strong field-aligned currents and optical aurora. Single-fluid MHD simulations in a dipole field with axisymmetric Alfvén speed, and the associated resonant toroidal Alfvén waves, were presented in Sakurai et al. (2022). The study was motivated by observations presented in the same paper, which found the Alfvén wave period modulated satellite electric and magnetic fields, ground magnetometer data, and optical auroral emissions. The simulation of this event aims to match the satellite and optical data and is shown in Figure 10.11. The flank magnetopause was driven by a burst of Kelvin-Helmholtz activity, which excited the fast mode in the magnetosphere that was then coupled to standing Alfvén waves. Panel (a) shows the predicted auroral emissions in a meridional plane at 6 MLT as a function of time. Note that the poleward motion of the arcs associated with phase mixing is in the opposite direction to those on PSBL field lines, as the Alfvén frequency decreases with latitude on the flank at these latitudes.

Figure 10.11(b,c) shows electric (E) and magnetic field (b) perturbations from a virtual satellite on the field line mapping to a latitude of 69.5° that sits in the center of the auroral emissions. The nodes of b corresponding to maxima of the upward field-aligned current are indicated by dashed red lines that also coincide with the peak emissions in panel (a) at 69.5°. Sakurai et al. (2022) also considered properties of the four arcs, such as the initial brightening and subsequent fading, and showed how these could be accounted for in terms of the decreasing phase-mixing length and reduction of Alfvén wave amplitude in time.

This could also explain the slight equatorward drift of the center of successive arcs, which was also seen in their optical data. The satellite data they reported was from a satellite on a field line that was at a higher latitude (71.68°) than the visible auroral arcs, and the corresponding virtual satellite E and b fields are shown in Figure 10.11(d,e). Although there are clearly Alfvén waves on this field line, there is no visible aurora at its footpoint as the thresholds of current and electron energy flux (1 μAm^2 and 1 mWm^2) required for the production of aurora are not met here (Chaston et al., 1091).

To consider the energetics of the process properly it is necessary to move beyond single fluid MHD, which neglects the electron mass. (This means the electrons can easily be accelerated along the field line to high speeds; however, they will have no kinetic energy, so a discussion of the energetics is not possible.) Sakurai et al. (2022) used two-fluid MHD to model the energy going into current-carrying electrons during the upward current (downgoing electron) phase and compared this with the magnetic energy of the Alfvén wave fields along the entire flux tube. They found the ratio was ~ 0.2, suggesting the Alfvén wave had plenty of energy to power the precipitation of the energetic electrons. However, over several cycles this could be a significant sink of Alfvén wave energy, unless the waves are continually driven by a fast wave (see Sections "Low-m Alfvén Waves" and 10.2.2).

Lysak and Song (2011) used a cartesian 3D two-fluid MHD simulation to focus on the electron acceleration that forms 1-2 R_e above the Earth. Their motivation was the nightside aurora that often forms on the PSBL field lines during a substorm. The large Alfvén speed gradients across the PSBL naturally lead to phase mixing and strong currents that are associated with electron fluxes capable of producing optical aurora (see Figure 10.2 and Wright and Allan (2008)). Lysak and Song (2011) show how the energization is associated with the formation of a parallel electric field formed by Landau damping.

Moving beyond the two-fluid approximation, a more complete model of electron energization can be achieved using a kinetic description of the electrons. There have been several recent studies using hybrid MHD-kinetic models in order to study auroral electron acceleration by FLRs. Damiano and Johnson (2012) performed the first simulation of the upward current region of a toroidal FLR using a 2-D hybrid MHD kinetic electron model in dipolar coordinates (Damiano et al., 2007). It was found that effects due to the magnetic mirror force (Knight, 1973; Nakamura, 2000) can accelerate electrons to energies on the order of a keV. The Alfvén wave energy dissipated by this acceleration would result in completely damping the resonance within 1–2 wave periods unless otherwise strongly driven, i.e., the electron acceleration is a major sink of FLR energy (consistent with the conclusions of
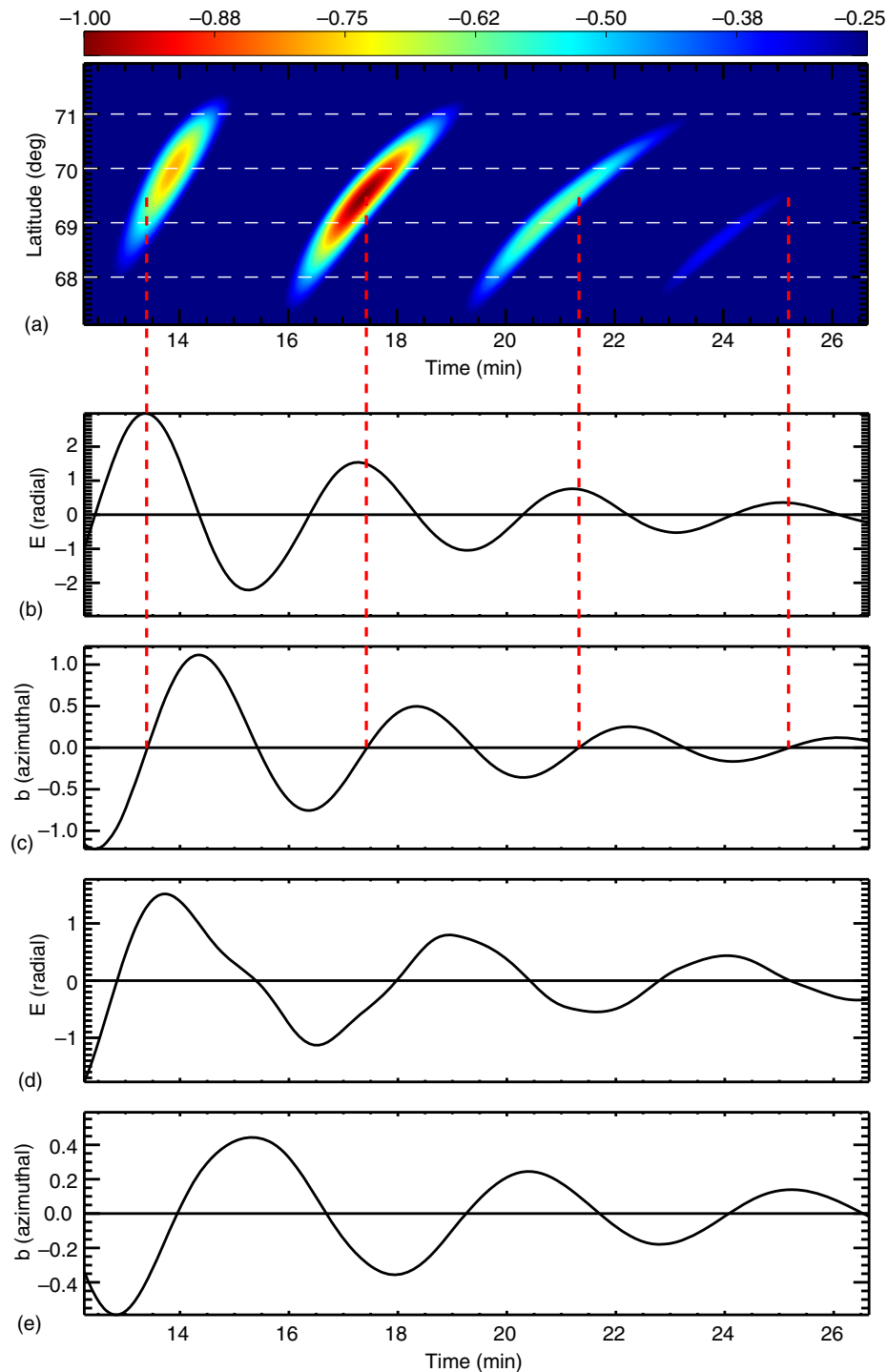
Figure 10.11 Simulation results of auroral arcs and satellite data. (a) Predicted auroral brightness keogram in a meridian plane at 6 MLT using downgoing electron energy flux as a proxy. The scale is normalized by 4 mWm². (b) and (c) show electric and magnetic fields measured by a virtual satellite on a field line mapping to a latitude of 69.5°. The dashed red lines correspond to maxima of the upward current. (d) and (e) are the same as (b) and (c), but for a field line mapping to 71.68°. Source: After Sakurai et al. (2022).

Sakurai et al. (2022) from using two-fluid theory). Similar results were found for electrons accelerated by poloidal modes (Damiano et al., 2019).

Follow-up studies included updating the numerical model to include further physical properties (Damiano et al., 2015), e.g., ion gyroradius effects (Damiano et al., 2016). This was aimed at understanding the ability of kinetic Alfvén waves originating from the plasma sheet to trap electrons and their effect on overall auroral electron precipitation. The authors found that electrons that are trapped in the source region of the wave can be carried significantly along the field line and thereby energized by the wave. However, this is sensitive to the ion temperature, with cold ions allowing for stronger trapping by the wave. A recent review summarizing these types of studies in the broad picture of the role of Alfvén waves in auroral electron acceleration can be found in Rankin et al. (2021).

10.3. EXTERNALLY DRIVEN (LOW-*m*) ALFVÉN WAVES

10.3.1. Energy Sources for Low-*m* Alfvén Waves

For an axisymmetric magnetosphere, two solutions for standing Alfvén waves exist. One is the toroidal mode, which corresponds to $m = 0$, and the other is the poloidal mode, which corresponds to $m = \infty$. In the real magnetosphere, these idealized cases do not occur, with $m \sim 10 - 20$ being a practical boundary between toroidal-type and poloidal-type waves.

Toroidal modes are driven by a variety of energy sources upstream of the dayside magnetosphere, including pressure disturbances in the solar wind, ion foreshock, and magnetosheath. Energy from the upstream region is then processed in several ways at the magnetopause boundary, including (1) a tendency to pass energy from lower-frequency disturbances to the magnetosphere and/or (2) the excitation and growth of several types of surface waves (Plaschke, 2016). This energy is also processed in the inhomogeneous medium of the Earth's magnetosphere, where intermediate global modes serve as band-pass filters for wave energy (Hwang & Sibeck, 2016), being excited at frequencies that depend on the properties of the magnetospheric cavity (wave speed, dimensions of the cavity, etc.). Ultimately, toroidal modes can be excited by upstream energy sources via many pathways in this multi-step process, including direct excitation from impulsive upstream disturbances that do not involve significant surface wave/global mode activity to situations involving intermediate wave modes. Perhaps the most well-known example of this is the classical field line resonance mechanism, where surface waves on the magnetopause couple resonantly to toroidal waves at specific locations in the magnetosphere that depend on the properties of the surface wave and the Alfvén speed distribution in the magnetosphere (Glassmeier et al., 1999). In any of these situations, the global properties of the toroidal modes depend on the wave modes involved, including their spatial extent and locations with peak wave amplitudes.

Enabled by multi-point ground-based and in situ measurements, recent observational work has focused on understanding the effect of the orientation and spatial scale of the upstream driver on the properties of the resulting toroidal waves. For example, Oliveira et al. (2020) presented results from satellite and ground-based magnetometer measurements suggesting that the impact angle of interplanetary shocks can affect a range of toroidal mode properties, including field-aligned mode structure, frequency, and amplitude; results from this study also suggest that the MLT of the shock impact may affect the local time extent of toroidal modes as indicated in the studies discussed in Section "Driver Properties", though additional observations at a wider range of MLT are needed to quantify this effect. B. Wang et al. (2020) showed global observations of waves with frequencies of a few mHz driven by ion foreshock transients; the waves excited had a range of m-values from 5 to 23 and exhibited a dawn-dusk asymmetry consistent with the location of the pressure disturbance in the ion foreshock. B. Wang et al. (2020) suggest the results could be consistent with a running pulse on the magnetopause leading to the generation of a waveguide mode (global mode) and ultimately to toroidal modes. B. Wang et al. (2022) examined the generation of Alfvén waves and other magnetospheric Ultra-Low-Frequency waves via magnetosheath jets, finding the associated ground magnetic disturbances are more localized and transient than waves typically excited by the solar wind, as expected for the more localized, shorter duration pulses that jets represent on the magnetopause. Sarris et al. (2022) used magnetic field measurements from two satellites with different orbital inclinations to quantify ULF wave power with distance from the magnetic equator, finding results overall consistent with expectations for the fundamental mode of low-m toroidal mode waves—less wave power in the azimuthal component of the magnetic field near the magnetic equator. Their dataset and approach could be adapted to study how wave power varies during symmetric and asymmetric driving conditions.

The earlier mentioned studies mostly focused on frequencies below 10 mHz. At higher frequencies, Takahashi and Heilig (2019) used a unique network of closely spaced ground-based magnetometers to show that a global mode generated by solar wind dynamic pressure variations drove multi-harmonic toroidal modes via field line resonance that exhibited rapid spatial variations in

latitude. The study demonstrates that closely spaced magnetometers can resolve the properties of Alfvén waves, including their latitude and time-dependent polarizations and phase speeds; the results also indicate that similarly closely spaced ground-based magnetometer observations can be used to separate transient from steady wave activity and examine phase mixing (Section "Driver Properties") and rapid changes in Alfvén wave polarization occurring near plumes (Section "Local Time Dependence and Plumes", Figure 10.3). Lena et al. (2021) used a unique satellite configuration (low-L perigee passes of the Van Allen Probes satellites near end of the mission) to detect multi-harmonic toroidal modes with frequencies of 0.5–3.5 Hz that were consistent with odd modes; their properties, including frequency and amplitude, varied from day to day, consistent with time-varying densities and driving conditions. Both the Takahashi and Heilig (2019) and Lena et al. (2021) studies indicate that more observations are needed at low-L values to understand the factors controlling high-frequency toroidal modes.

Though low-m waves tend to be excited by disturbances upstream of the dayside magnetosphere, these waves can also be excited via substorms and related phenomena on the nightside (see Sections "Magnetotail and Nightside Alfvén Waves" and "Outer Boundary and Waveguide/Cavity Modes"). For example, C.-P. Wang et al. (2022) found nightside Pi2 waves associated with plasma sheet disturbances that had polarizations consistent with toroidal modes. Takahashi et al. (2022) found nightside Pi2 waves can have low-m values or small phase shifts in longitude, consistent with a waveguide mode; furthermore, these waves often have mixed polarizations with significant wave power in the azimuthal magnetic field component away from the magnetic equator, consistent with the toroidal mode. More work is needed to understand Alfvén wave dynamics in the nightside magnetosphere, in particular the unique wave properties associated with (1) the stretched, often non-dipolar magnetic field geometry, (2) the range of possible spatial and temporal scales from bursty bulk flows, dipolarizing flux bundles, and other wave energy sources (e.g., m-values of 20–60 were reported in Liu et al., 2017), and (3) low ionospheric conductance.

Finally, whether excited by external or internal energy sources, low-m Alfvén waves are affected by the properties of the Alfvén speed profile (Section "Local Time Dependence and Plumes"). Recent observational work has shown that during active conditions with intense ring current, Alfvén speeds and frequencies (Sandhu et al., 2018; Wharton et al., 2020) are overall reduced. This leads to significant penetration of lower frequency wave energy, including low-m Alfvén waves, to the inner magnetosphere (Rae et al., 2019); this has important implications for several space weather impacts (see Section 10.5).

Additionally, Sandhu et al. (2021) observed that during geomagnetic storms, localized enhancements in ULF wave power (1–15 mHz) are often observed in the dusk sector and noted these enhancements may be associated with plasmaspheric plumes trapping fast mode wave energy as simulated by Degeling et al. (2018). As discussed in Section "Local Time Dependence and Plumes", the unique Alfvén speed spatial distribution in plume regions would have also been expected to alter Alfvén wave polarizations, amplitudes, and other properties.

10.3.2. Magnetoseismology

Externally driven toroidal waves are a valuable tool in estimating the magnetospheric mass density, denoted ρ_m. Based on the fact that the frequency of the waves depends only on the background magnetic field and the ρ_m distribution along it (see Equation (10.3)), we can determine ρ_m if we can measure the wave frequency and have good knowledge of the magnetic field and ρ_m distribution. This technique, now known as "magnetoseismology," was conceived a long time ago (e.g., Obayashi & Jacobs, 1958). With the ever-increasing amount of data from ground magnetometers (e.g., Del Corpo et al., 2019) and spacecraft experiments (e.g., Denton et al., 2022), magnetoseismic studies have become very common and practical for producing global mass density models. This is an important research area because the total mass density is difficult to determine with particle experiments.

The success of magnetoseismology depends on the efficiency and accuracy of frequency measurements. It is often difficult to determine the wave frequency in power spectra from a single ground magnetometer because the waves may be masked by various disturbances. The recognition that wave signals can be extracted by cross-spectral analysis of magnetic field data from two stations with a small latitudinal separation (Baransky et al., 1985; Waters et al., 1991) made a major contribution to the widespread use of magnetoseismology. The situation is different with spacecraft data. Toroidal waves in spacecraft data usually produce sharp spectral lines that are easy to identify. The challenge is to determine the harmonic mode number of each spectral line. The mode numbers can be reliably determined from the amplitude and phase relationship between electric and magnetic fields, along with theoretical models of standing wave structures (Takahashi & Denton, 2021).

The success of magnetoseismology also depends on the choice of magnetic field and field line mass distribution models. As for the magnetic field, a variety of empirical models have been derived from numerous observations in space and on the ground. One can choose an appropriate model depending on the location, solar wind condition, and geomagnetic activity level. The most

often used models are the dipole model, the International Geomagnetic Reference Field (IGRF) model appropriate for the inner magnetosphere, T89c (Tsyganenko, 1989) for sorting by Kp, and TS05 (Tsyganenko, 2002; Tsyganenko & Sitnov, 2005) for incorporating effects of the solar wind and the ring current. In the inner magnetosphere, the estimated mass density differs by up to 30% between the dipole and IGRF models (Berube et al., 2006). Models with no ring current effects lead to an overestimation of the mass density because the ring current reduces the equatorial magnetic field, thereby lowering the frequency of standing Alfvén waves (Vellante et al., 2014). When spacecraft data are used, this type of error can be reduced

by multiplying the magnitude of the model field by the ratio of the magnitudes of the measured and model fields (Denton et al., 2004).

In contrast, there are no field line mass distribution models directly derived from particle measurements. For this reason, the ratios between the harmonics of toroidal waves have been used to infer the field line mass distribution. Most often, the distribution is assumed to have a simple functional form: $\rho_m = \rho_{eq}(r_0/r)^p$, where r_0 is the equatorial distance to the field line, r is the distance to a point on the field line, and ρ_{eq} (equatorial mass density) and p (mass density power law index) are free parameters. The p value varies among the studies. For example, studies
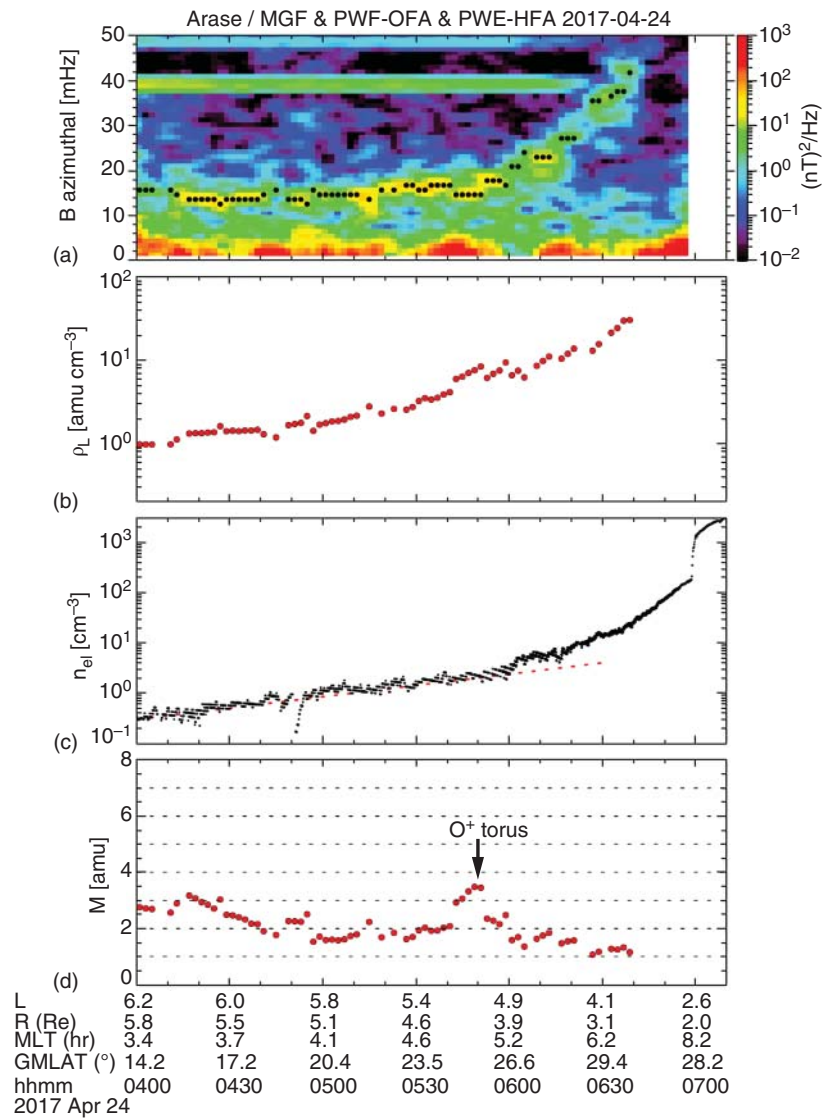
Figure 10.12 Magnetoseismic analysis of the O^+ torus at Arase (Nosé et al., 2018 /John Wiley & Sons). (a) Dynamic spectra of the azimuthal component of the magnetic field, showing spectral peaks (black dots) attributed to fundamental toroidal waves. (b) Mass density derived from the wave spectra. (c) Electron density. (d) Average ion mass. The peak marked by an arrowhead is attributed to an oxygen torus.

using spacecraft data obtained $p \sim 1$ (e.g., Denton et al., 2006), whereas a study using ground magnetometer data obtained $p \sim 4$ (Wharton et al., 2018). The discrepancy might be explained by the difference in how the fundamental and second harmonic frequencies are determined and incorporated into the modeling. These harmonics are the most sensitive to the density variation near the equator. Large uncertainties in their frequencies could lead to large errors in the estimated p.

Once ρ_m is determined, it can be combined with electron density (n_e) to gain information on the ion composition. n_e data are routinely produced when a spacecraft operates a sensitive plasma wave experiment (e.g., Kurth et al., 2015). We simply define the average ion mass M ($= \rho_m / n_e$) and use it as an indicator of heavy ion density. For a plasma consisting of H^+, He^+, and O^+, M takes a value somewhere between 1 amu (all H^+ plasma) and 16 amu (all O^+ plasma). As the He^+ density is relatively steady, the variability of M_i is attributed largely to the variability of the O^+ density (e.g., Del Corpo et al., 2022).

Variations of ρ_m and M occur on different time scales. A long-term variation occurs over a solar cycle (11-year period) due to the change in solar EV/EUV radiation, which controls the ionospheric feeding of O^+ ions into the magnetosphere (Takahashi et al., 2010). Short-time scale variations occur in association with geomagnetic storms and substorms (hours to days). When the geomagnetic activity is elevated, ionospheric O^+ ions are heated either in the polar region or at lower latitudes and transported to the inner magnetosphere. This process is considered to lead to the formation of an O^+ torus, possibly localized in longitude (Nosé et al., 2018). Figure 10.12 illustrates an example of a magnetoseismic analysis using data from the Arase spacecraft. The peak of M at 0550 UT ($L = 5.1$, Figure 10.12d) is attributed to the O^+ torus.

10.4. INTERNALLY DRIVEN (HIGH-*m*) ALFVÉN WAVES

Unlike externally excited toroidal waves, which commonly exhibit several harmonics, internally excited poloidal waves tend to have wave power concentrated in a single harmonic. The harmonic mode can be readily determined when we can measure the electric ($\delta \mathbf{E}$) and magnetic ($\delta \mathbf{B}$) fields of the waves. Theory predicts how the amplitude and phase of each field component change with distance from the magnetic equator. For example, the equator is the antinode of $\delta \mathbf{E}$ and a node of $\delta \mathbf{B}$ of odd harmonics (symmetric waves). The node-antinode relationship switches for even harmonics (antisymmetric waves). If we have a reliable estimate of the plasma mass density, we can also determine the harmonic mode from the wave frequency.

10.4.1. Symmetric Waves

Symmetric poloidal waves at the fundamental harmonic are excited in the ring current regions (see Section "High-m Alfvén Waves"), with a probability much lower than that of second harmonic poloidal waves. Theory had predicted that the symmetric waves can be excited through drift resonance $\omega - m\omega_d = 0$ when an inward gradient

$$\left. \frac{\partial F}{\partial L} \right|_{M,J} < 0, \qquad (10.8)$$

is established for the phase space density, F, of resonant ions, where ω is the wave frequency, m is the azimuthal wavenumber, ω_d is the particle drift frequency, and J is the second invariant of adiabatic particle motion (Chen & Hasegawa, 1991; Southwood, 1976). This circumstance requires a temporal effect in ring current dynamics because, in a steady state, the distribution is considered to be adiabatic, $\left. \frac{\partial F}{\partial L} \right|_{M,J} \approx 0$.

The first convincing evidence for the drift resonance instability was reported by Dai et al. (2013) in a study of a fundamental poloidal wave observed by the Van Allen Probe A spacecraft. Figure 10.13, taken from that study, shows that the poloidal field components (E_φ and B_r) oscillate with very regular waveforms and accompany equally regular oscillations in the flux of energetic ions. The amplitude and the phase of the particle flux oscillation depend on energy, and this feature was used to determine the resonance energy (90 kev) and the azimuthal wave number ($m \sim -70$). Most importantly, the ion phase space density evaluated at the magnetic moment for the resonance ions (in the range of 11–12 MeV/G) exhibited an inward gradient (the second invariant J was close to zero because the observation was made near the magnetic equator and a local pitch angle of 90° was considered). The same results for the phase space density were obtained for other fundamental poloidal wave events (Takahashi, Claudepierre, et al., 2018; Yamamoto et al., 2018).

An important finding from some of these spacecraft studies is that fundamental poloidal waves are the source of giant pulsations (Pgs) detected on the ground in magnetometer data (Takahashi, Claudepierre, et al., 2018; Yamamoto et al., 2018). Pgs have long been known for their highly monochromatic waveforms and other peculiar properties (Birkeland, 1901; Brekke et al., 1987; Sucksdorff, 1939). The origin of Pgs remained a mystery for some time, with both symmetric (Green, 1985; Takahashi et al., 1992) and antisymmetric poloidal waves (Chisham & Orr, 1991) considered as candidates. With unambiguous harmonic mode identification in space and multipoint ground magnetic field measurements around the footprints of the spacecraft (Takahashi et al.,
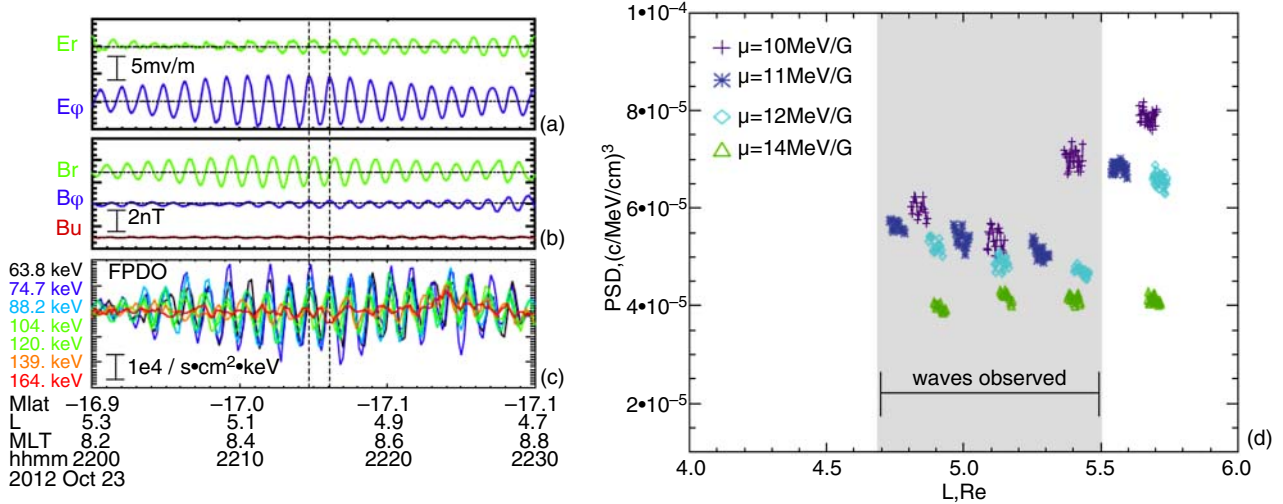
Figure 10.13 Data from the Van Allen Probe (RBSP)—A spacecraft for a fundamental poloidal wave event (Dai et al. (2013) /John Wiley & Sons). (a) Electric field radial (E_r) and azimuthal (E_φ) components. (b) Magnetic field components. B_μ denotes the compressional component. (c) Perturbation of the differential energy flux of ions at seven energy steps. (d) Ion phase space density at four values of magnetic moment are plotted as a function of the L value of the spacecraft.

2011), it now appears that Pgs are strictly associated with fundamental poloidal waves. However, we note that detection of fundamental poloidal waves with ground magnetometers is possible only when the magnitude of the azimuthal wave number is smaller than ∼50. A fundamental poloidal wave with a large azimuthal wave number was not detected on the ground (Takahashi et al., 2013), and there are apparently many high-m fundamental waves in the afternoon sector that are undetected on the ground (Brekke et al., 1987; Motoba et al., 2015).

10.4.2. Antisymmetric Waves

The most commonly observed poloidal waves have a second harmonic structure (Takahashi & McPherron, 1984). A theoretical prediction of the excitation of these waves has been made by considering instabilities involving the drift-bounce resonance

$$\omega - m\omega_d = N\omega_b \qquad (10.9)$$

of ring current particles with the waves, where ω_b is the particle bounce frequency and N is an integer specifying the harmonic order of bounce resonance. The wave frequency is assumed to be associated with a harmonic of standing Alfvén waves. According to Southwood and Hughes (1983), the instability condition is expressed as

$$\frac{dF}{dW} = \left.\frac{\partial F}{\partial W}\right|_{M,L} + \left(\frac{dL}{dW}\right)\left.\frac{\partial F}{\partial L}\right|_{M,W} > 0, \qquad (10.10)$$

where W is the particle energy, L is the magnetic field shell parameter (see Section "Low-m Alfvén Waves") and

M is the magnetic moment defined by $M = W\sin^2\alpha/B$ using the magnetic field magnitude B and the pitch angle α. An instability occurs either from energy inversion (a bump-on-tail structure), represented by the first term on the right-hand-side of the equation, or from a spatial gradient of the phase space density, represented by the second term. A bump-on-tail energetic ion distribution is commonly formed by the action of a time-dependent convection electric field (Ejiri et al., 1980). Note that the derivatives appearing on the right-hand-side of Equation (10.10) are to be evaluated for particles that are in resonance with the wave, i.e., satisfying Equation (10.9). Therefore, it is necessary to have information on the azimuthal wave number when using Equation (10.10) for instability analysis.

Recent spacecraft experiments made it possible to determine the m number and the ion phase space density required for instability analysis based on Equation 10.10. The m number can be determined using either multispacecraft phase delay analysis (Le et al., 2021; Takahashi, Oimatsu, et al., 2018) or ion finite Larmor radius sounding techniques (Min et al., 2017). These techniques indicate that m is negative (westward-porpagating waves) and has a magnitude of the order of 100. With such high m values, the ionospheric screening effect (Hughes & Southwood, 1976) is very strong, and ground magnetometers cannot detect the waves. One needs to use experiments such as a HF Doppler sounder (Wright & Yeoman, 1999) and HD radar (Shi et al., 2018; Yeoman & Wright, 2001) to detect the waves from the ground.

Once the m number is determined, the energies of resonant ions can be estimated using Equation (10.9) and the known relationship between the configuration of the background magnetic field and the particle guiding center drift (ω_d) and bounce (ω_b) frequencies (Hamlin et al., 1961; Yang et al., 2011). Typically, the solutions for the proton resonance energy are between ~10 keV and ~100 keV. The former is referred to as low-energy resonance or bounce resonance ($\omega \sim \omega_b$), while the latter is referred to as high-energy resonance ($m\omega_d \sim \omega_b$) (Southwood, 1976). It is possible to determine the relative importance of the two terms on the right hand side of Equation (10.10). In principle, this can be done for both resonance energies.

Figure 10.14 shows an analysis of the instability condition at the low-energy resonance for a second harmonic poloidal wave event observed by Van Allen Probes (RBSP-A and RBSP-B) (Takahashi, Oimatsu, et al., 2018). The proton distribution function F_{H+} exhibits a positive energy slope (Figure 10.14a) and an outward spatial gradient (Figure 10.14b). It is found that the first term has a larger magnitude and contributes to the instability. A positive energy slope ($\frac{\partial F}{\partial W} > 0$) at ~ 10 keV, resulting in a bump-on-tail energy distribution, is routinely formed by the combined action of the convection and corotation components of the global electric field in the magnetosphere (Ejiri et al., 1980). This is considered to be the reason for the ubiquitous presence of the second harmonic poloidal wave.

Figure 10.15 is a clear example of the association of a bump-on-tail energy distribution with second harmonic poloidal waves. This wave event was observed when the THEMIS-D spacecraft was moving outward in the outer plasmasphere, where a peak in the flux of ions was detected around 10 keV (Figure 10.15c). The dynamic spectra of the radial component of the magnetic field (Figure 10.15b) shows monochromatic spectral enhancement, with the peak changing from 20 mHz to 10 mHz as the spacecraft moved outward. The white trace is the frequency of the second harmonic poloidal wave computed using the electron density shown in Figure 10.15a. There is an excellent match between the bounce frequency (the red line in panel (b)) and the wave frequency (the white line) in support of the bounce resonance mechanism. A similar analysis has been done for the high-energy resonance (Oimatsu et al., 2018).

10.5. ROLE OF ALFVÉN WAVES IN SPACE WEATHER

Alfvén waves affect space weather in the terrestrial magnetosphere in a variety of ways, leading to potential impacts on human life and technology. This section will briefly review several ways that Alfvén waves impact space weather in order to (1) highlight gaps in our current understanding and modeling capabilities and (2) motivate future work and improvements in modeling and observational capabilities needed to account for these impacts in space weather models for nowcasts, climatology, etc.

Radiation belt and ring current particles are affected by Alfvén waves through a variety of interactions (Elkington & Sarris, 2016; Zong et al., 2017). These particles can cause unwanted charging on spacecraft in several ways, potentially leading to malfunctions and failures (Baker et al., 1998; Lanzerotti, 2001). For each wave-particle interaction, global and local effects on the particle populations depend in part on the wave amplitude, polarization, wave vector (m-number), and spatial extent; they also depend on the properties of the particles, including their global distribution at different energies, pitch angles,

RBSP-A HOPE Protons 2 March 2014
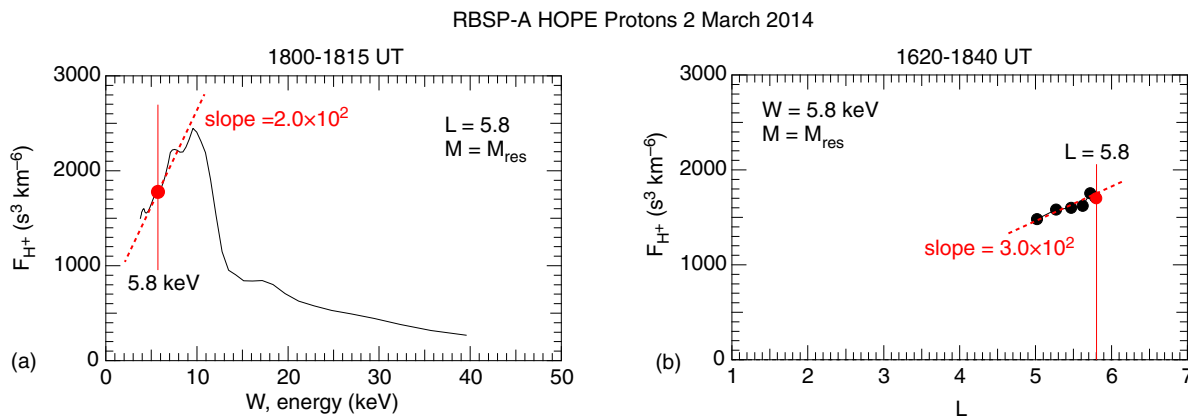
Figure 10.14 Analysis of particle data for a second-harmonic poloidal wave event (Oimatsu, et al., 2018 /John Wiley & Sons). (a) Proton phase space density plotted as a function of energy. The phase space density was calculated from the proton differential flux measured by the HOPE instrument on RBSP-A. (b) L dependence of the phase space density.
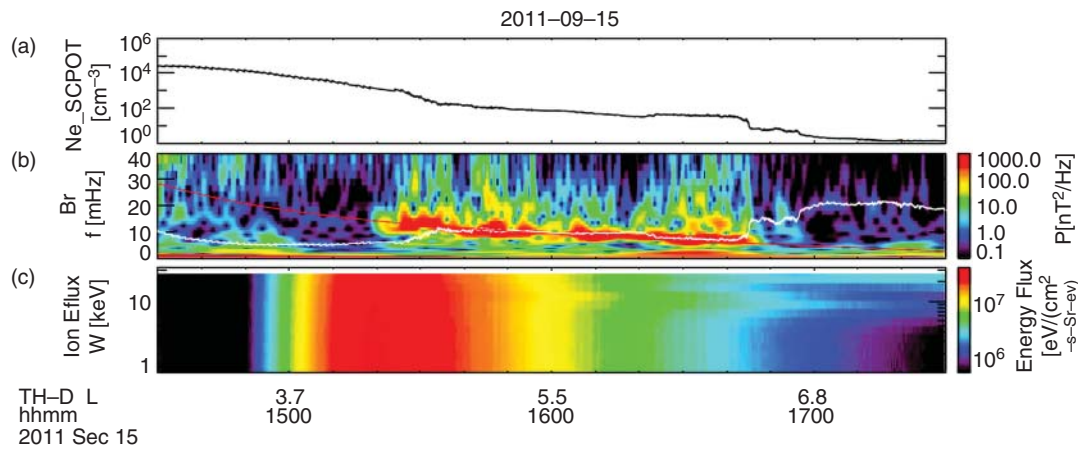
Figure 10.15 Data from the THEMIS-D spacecraft for a second harmonic poloidal wave event (Liu et al. (2013) /John Wiley & Sons). (a) Electron density is derived from the spacecraft potential. (b) Dynamic spectra of the radial component of the magnetic field. The white trace is the model second harmonic wave frequency estimated using the electron density and assuming an all-proton plasma. The red trace is the proton bounce frequency at the energy of the bump of the ion flux shown in panel (c). (c) Ion (assumed to be protons) differential energy flux.

etc. There are many unresolved questions concerning, e.g., the nature of ULF wave-particle interactions (Kress et al., 2012) and the relative importance of ULF waves versus other wave modes in affecting particle dynamics (Drozdov et al., 2022; Lejosne et al., 2022). In the context of this review, perhaps the most important unresolved question relates to how ULF wave-particle interactions are modified by non-uniform Alfvén wave fields and, more specifically, in 3D, non-dipole geometries. A few studies have examined how non-uniform wave fields affect particle dynamics, including local-time dependence of wave amplitude (Zhao et al., 2020), rapid phase changes near a resonance (Degeling et al., 2019), and the presence of multiple wave modes (Hao et al., 2020), but this remains a mostly unexplored research area with more work needed to understand the often complex particle dynamics that are observed. One major challenge originates from the fact that particle dynamics are usually treated in coordinate systems (Schulz & Lanzerotti, 1974) that differ significantly from coordinate systems used for organizing wave fields, particularly in the outer magnetosphere; ULF waves and particles can both be treated in dipole geometries with azimuthal symmetry, but, as discussed in this review, these geometries have significant limitations due to asymmetries caused by the magnetopause (Section "Outer Boundary and Waveguide/Cavity Modes"), plasma distribution (Section "Local Time Dependence and Plumes"), and driving conditions (Section "Driver Properties").

Alfvén waves also deposit energy in the ionosphere-thermosphere system (Greenwald & Walker, 1980; Newton et al., 1978) and can significantly modulate ionospheric electron densities (Belakhovsky et al., 2016).

These interactions, in turn, can cause (1) heating and thermospheric expansion (Crowley et al., 1985; Lathuillere et al., 1986; Verkhoglyadova et al., 2018) and potential loss of satellite tracking and/or unplanned, premature atmospheric reentry (Lin et al., 2022); (2) changes in ionospheric electron density that can in turn affect radio communication (Waters & Cox, 2009); and (3) changes in ionospheric electron density/conductance that in turn affect global magnetosphere-ionosphere dynamics (Buchert et al., 1999; Belakhovsky et al., 2016; Pilipenko et al., 2014). Broadly speaking, the ability of Alfvén waves to cause these effects depends on the amplitude of their ionospheric electric fields, the properties of precipitating particles associated with the Alfvén waves (Section 10.2.4), and the three-dimensional structure of the ambient ionosphere (altitude, longitude, and latitude—see Section "Ionospheric Boundaries"). There are numerous unresolved questions concerning the role of Alfvén waves in these three areas, including determining how their energy is deposited in the ionosphere-thermosphere system via electromagnetic versus kinetic (particle) energy and what conditions lead to the largest changes in ionospheric electron density/conductance. In the context of this review, it's important to determine what conditions lead to the largest magnetospheric electric field amplitudes, and thus the conditions that likely lead to the largest ionospheric electric field amplitudes.

Finally, Alfvén waves generate geomagnetic pulsations, which in turn induce geoelectric fields and can lead to geomagnetically induced currents (GIC). These GICs in turn cause disruptions in power systems that can lead to unwanted effects such as power outages and damage to transformers (Pilipenko, 2021;

Pulkkinen et al., 2017). The ability of Alfvén waves to generate large geomagnetically induced currents depends on their amplitudes, frequencies, polarizations, and spatial extents, as well as the ionospheric and ground conductivity and the properties of the power system of interest (Bedrosian & Love, 2015; Heyns et al., 2021; Yagova et al., 2021). There are still many unresolved questions concerning what conditions lead to the largest geomagnetically induced currents associated with Alfvén waves and other ULF wave modes, though there is a growing awareness that the ability of ULF waves (Hartinger et al., 2020; Shi et al., 2022) or any magnetosphere–ionosphere current system (Love et al., 2019; Lucas et al., 2020) to generate large-amplitude geomagnetically induced currents depends sensitively on the ground conductivity. In the context of this review, an important unresolved question concerns how large a GIC hazard Alfvén waves represent when compared to other ULF wave modes and other magnetosphere-ionosphere current systems. To address this, estimates of Alfvén wave amplitude, frequency, and polarization as a function of radial distance and magnetic local time should be obtained during active conditions; these are all needed as they all affect the resulting geoelectric fields and GIC. The frequency-dependent impedance related to local ground conductivity conditions should then be used to assess the hazard represented by Alfvén waves at different geographic locations (e.g., Bedrosian & Love, 2015).

Due to their space weather impacts, there is significant interest in developing global geospace models to a state where they can routinely produce hindcasts, nowcasts, and forecasts (based on upstream solar wind conditions and the current magnetospheric state) of the global properties of Alfvén waves and other Ultra-Low-Frequency waves in the Earth's magnetosphere (Hartinger et al., 2022). Achieving this goal will depend on future efforts in several areas, including increased observations needed to specify parameters for initial and boundary conditions such as Alfvén speed and ionospheric conductance, quantification of model uncertainty, identification and incorporation of missing physics (e.g., waves driven by drift-bounce resonance are not included in global MHD models), and quantification of numerical artifacts associated with grid resolution and other parameters.

10.6. CLOSING REMARKS

The extension of our knowledge of terrestrial Alfvén waves to other planetary magnetospheres and the solar corona provides exciting opportunities for generalizing theories to include extra physics that becomes important in these new settings and to observe their effects in data. Examples include the effects of rotation and the associated planetary disc, which provide density and current

distributions not present at Earth. A review of the fast and Alfvén modes of Jupiter's magnetosphere has been given recently by Lysak (2022), who shows how the ideas of FLRs and cavity modes can be adapted to this setting to include features that have no counterparts at Earth. There are also additional sources of Alfvén waves and aurora at Jupiter associated with the Galilean moons Io and Ganymede (Bagenal & Dols, 2020; Neubauer, 1980; Saur et al., 2018; Wright & Southwood, 1987).

At Saturn, the final phase of the Cassini mission included a series of proximal orbits inside of the planetary ring system. Evidence of persistent standing Alfvén waves was found, and these were interpreted as most likely driven by fast cavity modes, as the Alfvén waves have structure, familiar from FLRs at Earth (Southwood et al., 2021). The Hermean magnetosphere also shows evidence of standing Alfvén waves, and magneto-seismology developed in the terrestrial setting has been used to infer the plasma density distribution at Mercury (James et al., 2019).

Regarding Alfvén waves at Earth and in the solar corona, there is a complimentary aspect. In the corona, it is possible to image the global oscillations of a loop or arcade of field lines and develop ideas of the global behavior of various processes directly. However, it is not possible to record *in situ* measurements of fields and plasmas. The situation is reversed at Earth, where *in situ* measurements are possible but a global visualization of waves in the magnetosphere is not. The review by Nakariakov et al. (2016) compares and contrasts MHD waves in these two settings. They show how many processes are common to both, such as the resonant excitation of Alfvén waves driven by the fast mode. This process is thought to operate in loops and arcades and play a role in heating the corona. The use of waveguide and cavity modes is also relevant to the corona, which can have highly structured density features that are ordered by the equilibrium magnetic field. On dense filamentary structures, the kink mode can play the role of a cavity mode and provide a coherent driver for resonant Alfvén waves (Goossens et al., 2014). There are also similarities between the Earth's magnetotail and helmet streamers, and it is likely that the magnetotail waveguide and processes that operate in it may play a role in understanding features in the streamer and two ribbon flares. The interested reader is referred to the review by Nakariakov et al. (2016) for an in-depth discussion of the many other examples of similarities between terrestrial Alfvén waves and those in the solar corona.

ACKNOWLEDGMENTS

REFERENCES

Allan, W., & Knox, F. B. (1979, January). A dipole field model for axisymmetric Alfvén waves with finite ionosphere conductivities. *Planetary and Space Science*, 27(1), 79–85. doi: 10.1016/0032-0633(79)90149-1

Archer, M. O., Hartinger, M. D., Walsh, B. M., & Angelopoulos, V. (2017, January). Magnetospheric and solar wind dependences of coupled fast-mode resonances outside the plasmasphere. *Journal of Geophysical Research (Space Physics)*, 122, 212–226. doi: 10.1002/2016JA023428

Archer, M. O., Hartinger, M. D., Walsh, B. M., Plaschke, F., & Angelopoulos, V. (2015, December). Frequency variability of standing Alfvén waves excited by fast mode resonances in the outer magnetosphere. *Geophysical Research Letters*, 42, 10. doi: 10.1002/2015GL066683

Archer, M. O., Southwood, D. J., Hartinger, M. D., Rastaetter, L., & Wright, A. N. (2022, February). How a realistic magnetosphere alters the polarizations of surface, fast magnetosonic, and Alfvén waves. *Journal of Geophysical Research (Space Physics)*, 127(2), e2021JA030032. doi: 10.1029/2021JA030032

Bagenal, F., & Dols, V. (2020, May). The space environment of Io and Europa. *Journal of Geophysical Research (Space Physics)*, 125(5), e27485. doi: 10.1029/2019JA027485

Baker, D. N., Allen, J. H., Kanekal, S. G., & Reeves, G. D. (1998, January). Disturbed space environment may have been related to pager satellite failure. *EOS Transactions*, 79(40), 477–477. doi: 10.1029/98EO00359

Baransky, L. N., Borovkov, J. E., Gokhberg, M. B., Krylov, S. M., & Troitskaya, V. A. (1985). High-resolution method of direct measurement of the magnetic-field lines eigen frequencies. *Planetary and Space Science*, 33(12), 1369–1374. doi: 10.1016/0032-0633(85)90112-6

Bedrosian, P. A., & Love, J. J. (2015, December). Mapping geoelectric fields during magnetic storms: Synthetic analysis of empirical United States impedances. *Geophysical Research Letters*, 42(23), 10,160–10,170. doi: 10.1002/2015GL066636

Belakhovsky, V., Pilipenko, V., Murr, D., Fedorov, E., & Kozlovsky, A. (2016, June). Modulation of the ionosphere by Pc5 waves observed simultaneously by GPS/TEC and EISCAT. *Earth, Planets and Space*, 68(1), 102. doi: 10.1186/s40623-016-0480-7

Berube, D., Moldwin, M. B., & Ahn, M. (2006). Computing magnetospheric mass density from field line resonances in a realistic magnetic field geometry. *Journal of Geophysical Research*, 111(A8), A08206. doi: 10.1029/2005ja011450

Birkeland, K. (1901). Expédition norvégienne de 1899–1900 pour l'étude des aurores boréales. Résultats des recherches magnétiques. *Videnskabsselskabets Skrifter, I. Mathematisk-naturvidenskabelig klasse, Christiania*, 1, 1–80.

Brekke, A., Feder, T., & Berger, S. (1987). Pc4 giant pulsations recorded in Tromsø, 1929–1985. *Journal of Atmospheric and Terrestrial Physics*, 49(10), 1027–1032. doi: 10.1016/0021-9169(87)90109-7

Buchert, S. C., Fujii, R., & Glassmeier, K. H. (1999, May). Ionospheric conductivity modulation in ULF pulsations. *Journal of Geophysical Research*, 104(A5), 10,119–10,134. doi: 10.1029/1998JA900180

Chaston, C. C., Peticolas, L. M., Bonnell, J. W., Carlson, C. W., Ergun, R. E., McFadden, J. P., & Strangeway, R. J. (2003, February). Width and brightness of auroral arcs driven by inertial Alfven waves. *Journal of Geophysical Research (Space Physics)*, 108(A2), 1091. doi: 10.1029/2001JA007537

Chen, L., & Hasegawa, A. (1974, March). A theory of long-period magnetic pulsations: 1. Steady state excitation of field line resonance. *Journal of Geophysical Research*, 79, 1024–1032. doi: 10.1029/JA079i007p01024

Chen, L., & Hasegawa, A. (1991). Kinetic-theory of geomagnetic-pulsations.1. Internal excitations by energetic particles. *Journal of Geophysical Research: Space Physics*, 96(A2), 1503–1512. doi: 10.1029/90ja02346

Chisham, G., & Orr, D. (1991, July). Statistical studies of giant pulsations (Pgs): Harmonic mode. *Planetary and Space Science*, 39(7), 999–1006. doi: 10.1016/0032-0633(91)90105-J

Choi, J., & Lee, D.-H. (2021). On the persistent poloidal Alfven waves. *Geophysical Research Letters*, 48(12), e2021GL092945. Retrieved from https://agupubs.onlinelibrary.wiley.com/doi/abs/10.1029/2021GL092945 (e2021GL092945 2021GL092945) doi: https://doi.org/10.1029/2021GL092945

Claudepierre, S. G., Hudson, M. K., Lotko, W., Lyon, J. G., & Denton, R. E. (2010, November). Solar wind driving of magnetospheric ULF waves: Field line resonances driven by dynamic pressure fluctuations. *Journal of Geophysical Research (Space Physics)*, 115, A11202. doi: 10.1029/2010JA015399

Claudepierre, S. G., Toffoletto, F. R., & Wiltberger, M. (2016, January). Global MHD modeling of resonant ULF waves: Simulations with and without a plasmasphere. *Journal of Geophysical Research (Space Physics)*, 121(1), 227–244. doi: 10.1002/2015JA022048

Crowley, G., Wade, N., Waldock, J. A., Robinson, T. R., & Jones, T. B. (1985, August). High time-resolution observations of periodic frictional heating associated with a Pc5 micropulsation. *Nature*, 316(6028), 528–530. doi: 10.1038/316528a0

Dai, L., Takahashi, K., Wygant, J. R., Chen, L., Bonnell, J., Cattell, C. A., et al. (2013, August). Excitation of poloidal standing Alfvén waves through drift resonance wave-particle interaction. *Geophysical Research Letters*, 40(16), 4127–4132. doi: 10.1002/grl.50800

Damiano, P. A., & Johnson, J. R. (2012). Electron acceleration in a geomagnetic field line resonance. *Geophysical Research Letters*, 39(2). Retrieved from https://agupubs.onlinelibrary.wiley.com/doi/abs/10.1029/2011GL050264 doi: https://doi.org/10.1029/2011GL050264

Damiano, P. A., Johnson, J. R., & Chaston, C. C. (2015). Ion temperature effects on magnetotail Alfvén wave propagation and electron energization. *Journal of Geophysical Research: Space Physics*, *120*(7), 5623–5632. Retrieved from https://agupubs.onlinelibrary.wiley.com/doi/abs/10.1002/2015JA021074 doi: https://doi.org/10.1002/2015JA021074

Damiano, P. A., Johnson, J. R., & Chaston, C. C. (2016). Ion gyroradius effects on particle trapping in kinetic Alfvén waves along auroral field lines. *Journal of Geophysical Research: Space Physics*, *121*(11), 10,831–10,844. Retrieved from https://agupubs.onlinelibrary.wiley.com/doi/abs/10.1002/2016JA022566 doi: https://doi.org/10.1002/2016JA022566

Damiano, P. A., Kim, E. H., Johnson, J. R., & Porazik, P. (2019, August). Electron energization by parallel electric fields in poloidal standing waves. *Journal of Geophysical Research (Space Physics)*, *124*(8), 6691–6700. doi: 10.1029/2019JA026849

Damiano, P. A., Wright, A. N., Sydora, R. D., & Samson, J. C. (2007, June). Energy dissipation via electron energization in standing shear Alfvén waves. *Physics of Plasmas*, *14*(6), 062904. doi: 10.1063/1.2744226

Degeling, A. W., Rae, I. J., Watt, C. E. J., Shi, Q. Q., Rankin, R., & Zong, Q. G. (2018, February). Control of ULF wave accessibility to the inner magnetosphere by the convection of plasma density. *Journal of Geophysical Research (Space Physics)*, *123*(2), 1086–1099. doi: 10.1002/2017JA024874

Degeling, A. W., & Rankin, R. (2008). Resonant drift echoes in electron phase space density produced by dayside pc5 waves following a geomagnetic storm. *Journal of Geophysical Research: Space Physics*, *113*(A10). doi: 10.1029/2008JA013254

Degeling, A. W., Rankin, R., Kabin, K., Rae, I. J., & Fenrich, F. R. (2010, October). Modeling ULF waves in a compressed dipole magnetic field. *Journal of Geophysical Research (Space Physics)*, *115*, A10212. doi: 10.1029/2010JA015410

Degeling, A. W., Rankin, R., Wang, Y., Shi, Q. Q., & Zong, Q.-G. (2019). Alteration of particle drift resonance dynamics near poloidal mode field line resonance structures. *Journal of Geophysical Research: Space Physics*, *124*(9), 7385–7401. doi: 10.1029/2019JA026946

Del Corpo, A., Vellante, M., Heilig, B., Pietropaolo, E., Reda, J., & Lichtenberger, J. (2019). Observing the cold plasma in the Earth's magnetosphere with the EMMA network. *Annals of Geophysics*, *62*(4). doi: 10.4401/ag-7751

Del Corpo, A., Vellante, M., Zhelavskaya, I. S., Shprits, Y. Y., Heilig, B., Reda, J., et al. (2022). Study of the average ion mass of the dayside magnetospheric plasma. *Journal of Geophysical Research: Space Physics*. *127*(7), A030605. doi: 10.1029/2022ja030605

Denton, R. E., Lessard, M. R., & Kistler, L. M. (2003, March). Radial localization of magnetospheric guided poloidal Pc 4-5 waves. *Journal of Geophysical Research (Space Physics)*, *108*(A3), 1105. doi: 10.1029/2002JA009679

Denton, R. E., Takahashi, K., Anderson, R. R., & Wuest, M. P. (2004). Magnetospheric toroidal Alfvén wave harmonics and the field line distribution of mass density. *Journal of Geophysical Research*, *109*(A6), A06202. doi: 10.1029/2003ja010201

Denton, R. E., Takahashi, K., Galkin, I. A., Nsumei, P. A., Huang, X., Reinisch, B. W., et al. (2006). Distribution of density along magnetospheric field lines. *Journal of Geophysical Research*, *111*(A4), A04213. doi: 10.1029/2005ja011414

Denton, R. E., Takahashi, K., Min, K., Hartley, D. P., Nishimura, Y., & Digman, M. C. (2022). Models for magnetospheric mass density and average ion mass including radial dependence. *Frontiers in Astronomy and Space Sciences*, *9*. doi: 10.3389/fspas.2022.1049684

Drozdov, A. Y., Blum, L. W., Hartinger, M., Zhao, H., Lejosne, S., Hudson, M. K., et al. (2022, February). Radial transport versus local acceleration: The long-standing debate. *Earth and Space Science*, *9*(2), e02216. doi: 10.1029/2022EA002216

Duan, S., Dai, L., & Wang, C. (2022, December). Kinetic Alfvén waves in the magnetotail during substorms. *Reviews of Modern Plasma Physics*, *6*(1), 40. doi: 10.1007/s41614-022-00100-5

Ejiri, M., Hoffman, R. A., & Smith, P. H. (1980). Energetic particle penetrations into the inner magnetosphere. *Journal of Geophysical Research*, *85*(A2), 653. doi: 10.1029/JA085iA02p00653

Elkington, S. R., & Sarris, T. E. (2016, 11). The role of Pc-5 ULF waves in the radiation belts: Current understanding and open questions. In *Waves, Particles, and Storms in Geospace: A Complex Interplay*. Oxford University Press. Retrieved from https://doi.org/10.1093/acprof:oso/9780198705246.003.0005 doi: 10.1093/acprof:oso/9780198705246.003.0005

Ellington, S. M., Moldwin, M. B., & Liemohn, M. W. (2016, March). Local time asymmetries and toroidal field line resonances: Global magnetospheric modeling in SWMF. *Journal of Geophysical Research (Space Physics)*, *121*(3), 2033–2045. doi: 10.1002/2015JA021920

Elsden, T. (2016). *Numerical Modelling of Ultra Low Frequency Waves in Earth's Magnetosphere* (Doctoral dissertation, University of St Andrews). doi: http://hdl.handle.net/10023/15663

Elsden, T., Wright, A., & Degeling, A. (2022, September). A review of the theory of 3-D Alfvén (field line) resonances. *Frontiers in Astronomy and Space Sciences*, *9*, 917817. doi: 10.3389/fspas.2022.917817

Elsden, T., & Wright, A. N. (2017, March). The theoretical foundation of 3-D Alfvén resonances: Time-dependent solutions. *Journal of Geophysical Research (Space Physics)*, *122*, 3247–3261. doi: 10.1002/2016JA023811

Elsden, T., & Wright, A. N. (2018, January). The broadband excitation of 3-D Alfvén resonances in a MHD waveguide. *Journal of Geophysical Research (Space Physics)*, *123*, 530–547. doi: 10.1002/2017JA025018

Elsden, T., & Wright, A. N. (2019, January). The effect of fast normal mode structure and magnetopause forcing on FLRs in a 3-D waveguide. *Journal of Geophysical Research (Space Physics)*, *124*(1), 178–196. doi: 10.1029/2018JA026222

Elsden, T., & Wright, A. N. (2020, August). Evolution of high-m poloidal Alfvén waves in a dipole magnetic field. *Journal of Geophysical Research (Space Physics)*, *125*(8), e28187. doi: 10.1029/2020JA028187

Elsden, T., & Wright, A. N. (2022, February). Polarization properties of 3-D field line resonances. *Journal of Geophysical Research (Space Physics)*, *127*(2), e30080. doi: 10.1029/2021JA030080

Glassmeier, K.-H., Othmer, C., Cramm, R., Stellmacher, M., & Engebretson, M. (1999, January). Magnetospheric field line

resonances: A comparative planetology approach. *Surveys in Geophysics*, *20*(1), 61–109. doi: 10.1023/A:1006659717963

Goossens, M., Soler, R., Terradas, J., Van Doorsselaere, T., & Verth, G. (2014, June). The transverse and rotational motions of magnetohydrodynamic kink waves in the solar atmosphere. *Astrophysical Journal*, *788*(1), 9. doi: 10.1088/0004-637X/788/1/9

Green, C. A. (1985). Giant pulsations in the plasmasphere. *Planetary and Space Science*, *33*(10), 1155–1168. doi: 10.1016/0032-0633(85)90073-x

Greenwald, R. A., & Walker, A. D. M. (1980, October). Energetics of long period resonant hydromagnetic waves. *Geophysical Research Letters*, *7*(10), 745–748. doi: 10.1029/GL007i010p00745

Hamlin, D. A., Karplus, R., Vik, R. C., & Watson, K. M. (1961). Mirror and azimuthal drift frequencies for geomagnetically trapped particles. *Journal of Geophysical Research*, *66*(1), 1–4. doi: 10.1029/JZ066i001p00001

Hao, Y. X., Zhao, X. X., Zong, Q.-G., Zhou, X.-Z., Rankin, R., Chen, X. R., et al. (2020). Simultaneous observations of localized and global drift resonance. *Geophysical Research Letters*, *47*(17). doi: 10.1029/2020GL088019

Hartinger, M. D., Shi, X., Lucas, G. M., Murphy, B. S., Kelbert, A., Baker, J. B. H., et al. (2020, September). Simultaneous observations of geoelectric and geomagnetic fields produced by magnetospheric ULF waves. *Geophysical Research Letters*, *47*(18), e89441. doi: 10.1029/2020GL089441

Hartinger, M. D., Takahashi, K., Drozdov, A. Y., Shi, X., Usanova, M. E., & Kress, B. (2022, April). ULF wave modeling, effects, and applications: Accomplishments, recent advances, and future. *Frontiers in Astronomy and Space Sciences*, *9*, 867394. doi: 10.3389/fspas.2022.867394

Heyns, M. J., Lotz, S. I., & Gaunt, C. T. (2021, February). Geomagnetic pulsations driving geomagnetically induced currents. *Space Weather*, *19*(2), e2020SW002557. doi: 10.1029/2020SW002557

Heyvaerts, J., & Priest, E. R. (1983, January). Coronal heating by phase-mixed shear Alfven waves. *Astronomy and Astrophysics*, *117*, 220–234.

Hughes, W. J., & Southwood, D. J. (1976, July). The screening of micropulsation signals by the atmosphere and ionosphere. *Journal of Geophysical Research*, *81*(19), 3234. doi: 10.1029/JA081i019p03234

Hwang, K. J., & Sibeck, D. G. (2016, February). Role of low-frequency boundary waves in the dynamics of the dayside magnetopause and the inner magnetosphere. *Washington DC American, Geophysical Union Geophysical Monograph Senes*, *216*, 213–239. doi: 10.1002/9781119055006.ch13

Jacobs, J. A., Kato, Y., Matsushita, S., & Troitskaya, V. A. (1964, January). Classification of geomagnetic micropulsations. *Journal of Geophysical Research*, *69*, 180–181. doi: 10.1029/JZ069i001p00180

James, M. K., Imber, S. M., Yeoman, T. K., & Bunce, E. J. (2019, January). Field line resonance in the Hermean magnetosphere: Structure and implications for plasma distribution. *Journal of Geophysical Research (Space Physics)*, *124*(1), 211–228. doi: 10.1029/2018JA025920

Keiling, A. (2009, February). Alfvén waves and their roles in the dynamics of the Earth's magnetotail: A review. *Space Science Reviews*, *142*(1-4), 73–156. doi: 10.1007/s11214-008-9463-8

Keiling, A., & Takahashi, K. (2011, November). Review of Pi2 Models. *Space Science Reviews*, *161*(1-4), 63–148. doi: 10.1007/s11214-011-9818-4

Kivelson, M. G., & Russell, C. T. (1995). *Introduction to Space Physics*. 586. ISBN 0521451043. Cambridge, UK: Cambridge University Press.

Kivelson, M. G., & Southwood, D. J. (1986, April). Coupling of global magnetospheric MHD eigenmodes to field line resonances. *Journal of Geophysical Research*, *91*, 4345–4351. doi: 10.1029/JA091iA04p04345

Klimushkin, D. Y., Leonovich, A. S., & Mazur, V. A. (1995, June). On the propagation of transversely small-scale standing Alfven waves in a three-dimensionally inhomogeneous magnetosphere. *Journal of Geophysical Research*, *100*(A6), 9527–9534. doi: 10.1029/94JA03233

Knight, S. (1973, May). Parallel electric fields. *Planetary and Space Science*, *21*(5), 741–750. doi: 10.1016/0032-0633(73)90093-7

Kress, B. T., Hudson, M. K., Ukhorskiy, A. Y., & Mueller, H.-R. (2012). Nonlinear radial transport in the earth's radiation belts. In D. Summers, I. R. Mann, D. N. Baker & M. Schulz (Eds.). *Dynamics of the earth's radiation belts and inner magnetosphere* (151–160). American Geophysical Union (AGU). doi: https://doi.org/10.1029/2012GM001333

Kurth, W. S., De Pascuale, S., Faden, J. B., Kletzing, C. A., Hospodarsky, G. B., Thaller, S., & Wygant, J. R. (2015). Electron densities inferred from plasma wave spectra obtained by the waves instrument on van allen probes. *Journal of Geophysical Research: Space Physics*, *120*(2), 904–914. doi: 10.1002/2014JA020857

Lambour, R. L., Weiss, L. A., Elphic, R. C., & Thomsen, M. F. (1997, October). Global modeling of the plasmasphere following storm sudden commencements. *Journal of Geophysical Research*, *102*(A11), 24351–24368. doi: 10.1029/97JA02037

Lanzerotti, L. J. (2001, January). Space weather effects on technologies. *Washington DC American Geophysical Union Geophysical Monograph Series*, *125*, 11–22. doi: 10.1029/GM125p0011

Lathuillere, C., Glangeaud, F., & Zhao, Z. Y. (1986, February). Ionospheric ion heating by ULF Pc 5 magnetic pulsations. *Journal of Geophysical Research*, *91*(A2), 1619–1626. doi: 10.1029/JA091iA02p01619

Le, G., Chi, P. J., Strangeway, R. J., Russell, C. T., Slavin, J. A., Anderson, B., et al. (2021, May). MMS observations of field line resonances under disturbed solar wind conditions. *Journal of Geophysical Research (Space Physics)*, *126*(5), e28936. doi: 10.1029/2020JA028936

Le, G., Chi, P. J., Strangeway, R. J., Russell, C. T., Slavin, J. A., Takahashi, K., et al. (2017, April). Global observations of magnetospheric high-m poloidal waves during the 22 June 2015 magnetic storm. *Geophysical Research Letters*, *44*(8), 3456–3464. doi: 10.1002/2017GL073048

Lejosne, S., Allison, H. J., Blum, L. W., Drozdov, A. Y., Hartinger, M. D., Hudson, M. K., et al. (2022, June). Differentiating between the leading processes for electron radiation belt acceleration. *Frontiers in Astronomy and Space Sciences*, *9*, 896245. doi: 10.3389/fspas.2022.896245

Lena, F. R., Ozeke, L. G., Wygant, J. R., Tian, S., Breneman, A. W., & Mann, I. R. (2021, January). Detection of Hertz frequency multiharmonic field line resonances at Low-L (L = 1.1-1.5) during Van Allen probe perigee passes. *Geophysical Research Letters*, 48(1), e0632. doi: 10.1029/2020GL090632

Leonovich, A. S., Klimushkin, D. Y., & Mager, P. N. (2015, July). Experimental evidence for the existence of monochromatic transverse small-scale standing Alfvén waves with spatially dependent polarization. *Journal of Geophysical Research (Space Physics)*, 120(7), 5443–5454. doi: 10.1002/2015JA021044

Leonovich, A. S., & Mazur, V. A. (1993, Sep). A theory of transverse small-scale standing Alfvén waves in an axially symmetric magnetosphere. *Planetary and Space Science*, 41(9), 697–717. doi: 10.1016/0032-0633(93)90055-7

Lin, D., Wang, W., Garcia-Sage, K., Yue, J., Merkin, V., Mclnerney, J. M., et al. (2022, December). Thermospheric neutral density variation during the "SpaceX" storm: Implications from physics-based whole Geospace modeling. *Space Weather*, 20(12), e2022SW003254. doi: 10.1029/2022SW003254

Liu, J., Angelopoulos, V., Zhang, X. J., Runov, A., Artemyev, A., Plaschke, F., et al. (2017, October). Ultralow frequency waves deep inside the inner magnetosphere driven by dipolarizing flux bundles. *Journal of Geophysical Research (Space Physics)*, 122(10), 10,112–10,128. doi: 10.1002/2017JA024270

Liu, W., Cao, J. B., Li, X., Sarris, T. E., Zong, Q. G., Hartinger, M., et al. (2013). Poloidal ULF wave observed in the plasmasphere boundary layer. *Journal of Geophysical Research: Space Physics*, 118(7), 4298–4307. doi: 10.1002/jgra.50427

Love, J. J., Lucas, G. M., Bedrosian, P. A., & Kelbert, A. (2019, March). Extreme-value geoelectric amplitude and polarization across the northeast United States. *Space Weather*, 17(3), 379–395. doi: 10.1029/2018SW002068

Lucas, G. M., Love, J. J., Kelbert, A., Bedrosian, P. A., & Rigler, E. J. (2020, February). A 100-year geoelectric hazard analysis for the U.S. high-voltage power grid. *Space Weather*, 18(2), e02329. doi: 10.1029/2019SW002329

Lyon, J. G., Fedder, J. A., & Mobarry, C. M. (2004, October). The Lyon-Fedder-Mobarry (LFM) global MHD magnetospheric simulation code. *Journal of Atmospheric and Solar-Terrestrial Physics*, 66(15-16), 1333–1350. doi: 10.1016/j.jastp.2004.03.020

Lysak, R. L. (2022, June). Field line resonances and cavity modes at Earth and Jupiter. *Frontiers in Astronomy and Space Sciences*, 9, 913554. doi: 10.3389/fspas.2022.913554

Lysak, R. L., & Song, Y. (2011, September). Development of parallel electric fields at the plasma sheet boundary layer. *Journal of Geophysical Research (Space Physics)*, 116, A00K14. doi: 10.1029/2010JA016424

Lysak, R. L., Song, Y., Sciffer, M. D., & Waters, C. L. (2015, January). Propagation of Pi2 pulsations in a dipole model of the magnetosphere. *Journal of Geophysical Research (Space Physics)*, 120(1), 355–367. doi: 10.1002/2014JA020625

Lysak, R. L., Song, Y., Waters, C. L., Sciffer, M. D., & Obana, Y. (2020, July). Numerical investigations of interhemispheric asymmetry due to ionospheric conductance. *Journal of Geophysical Research (Space Physics)*, 125(7), e27866. doi: 10.1029/2020JA027866

Mager, P. N., & Klimushkin, D. Y. (2021, January). The field line resonance in the three dimensionally inhomogeneous magnetosphere: Principal features. *Journal of Geophysical Research (Space Physics)*, 126(1), e28455. doi: 10.1029/2020JA028455

Mann, I. R., & Wright, A. N. (1995, December). Finite lifetimes of ideal poloidal Alfvén waves. *Journal of Geophysical Research*, 100, 23677–23686. doi: 10.1029/95JA02689

Mann, I. R., Wright, A. N., & Cally, P. S. (1995, October). Coupling of magnetospheric cavity modes to field line resonances: A study of resonance widths. *Journal of Geophysical Research*, 100, 19441–19456. doi: 10.1029/95JA00820

Min, K., Takahashi, K., Ukhorskiy, A. Y., Manweiler, J. W., Spence, H. E., Singer, J., et al. (2017, March). Second harmonic poloidal waves observed by Van Allen Probes in the dusk-midnight sector. *Journal of Geophysical Research (Space Physics)*, 122(3), 3013–3039. doi: 10.1002/2016JA023770

Motoba, T., Takahashi, K., Rodriguez, J. V., & Russell, C. T. (2015). Giant pulsations on the afternoonside: Geostationary satellite and ground observations. *Journal of Geophysical Research: Space Physics*, 120. doi: 10.1002/2015ja021592

Nakamura, T. K. (2000, May). Parallel electric field of a mirror kinetic Alfvén wave. *Journal of Geophysical Research*, 105(A5), 10729–10738. doi: 10.1029/1999JA900494

Nakariakov, V. M., Pilipenko, V., Heilig, B., Jelínek, P., Karlicky, M., Klimushkin, D. Y., et al. (2016, April). Magnetohydrodynamic oscillations in the solar corona and Earth's magnetosphere: Towards consolidated understanding. *Space Science Reviews*, 200(1-4), 75–203. doi: 10.1007/s11214-015-0233-0

Neubauer, F. M. (1980, March). Nonlinear standing Alfvén wave current system at Io: Theory. *Journal of Geophysical Research*, 85(A3), 1171–1178. doi: 10.1029/JA085iA03p01171

Newton, R. S., Southwood, D. J., & Hughes, W. J. (1978, March). Damping of geomagnetic pulsations by the ionosphere. *Planetary and Space Science*, 26(3), 201–209. doi: 10.1016/0032-0633(78)90085-5

Nosé, M., Matsuoka, A., Kumamoto, A., Kasahara, Y., Goldstein, J., Teramoto, M., et al. (2018). Longitudinal structure of oxygen torus in the inner magnetosphere: Simultaneous observations by arase and van allen probe a. *Geophysical Research Letters*, 45(19), 10,177–10,184. doi: 10.1029/2018gl080122

Obana, Y., Waters, C. L., Sciffer, M. D., Menk, F. W., Lysak, R. L., Shiokawa, K., et al. (2015, June). Resonance structure and mode transition of quarter-wave ULF pulsations around the dawn terminator. *Journal of Geophysical Research (Space Physics)*, 120(6), 4194–4212. doi: 10.1002/2015JA021096

Obayashi, T., & Jacobs, J. A. (1958). Geomagnetic pulsations and the Earth's outer atmosphere. *Geophysical Journal International*, 1(1), 53–63. doi: 10.1111/j.1365-246X.1958.tb00034.x

Oimatsu, S., Nose, M., Takahashi, K., Yamamoto, K., Keika, K., Kletzing, C. A., et al. (2018). Van Allen Probes observations of drift-bounce resonance and energy transfer between energetic ring current protons and poloidal Pc4 wave. *Journal of Geophysical Research: Space Physics*. 123(5), 3421–3435.

Oliveira, D. M., Hartinger, M. D., Xu, Z., Zesta, E., Pilipenko, V. A., Giles, B. L., & Silveira, M. V. D. (2020, December). Interplanetary shock impact angles control magnetospheric ULF wave activity: Wave amplitude, frequency, and power

spectra. *Geophysical Research Letters*, *47*(24), e90857. doi: 10.1029/2020GL090857

Pilipenko, V. (2021, September). Space weather impact on ground-based technological systems. *Solar-Terrestrial Physics*, *7*(3), 68–104. doi: 10.12737/stp-73202106

Pilipenko, V., Belakhovsky, V., Kozlovsky, A., Fedorov, E., & Kauristie, K. (2014). Ulf wave modulation of the ionospheric parameters: Radar and magnetometer observations. *Journal of Atmospheric and Solar-Terrestrial Physics*, *108*, 68–76. Retrieved from https://www.sciencedirect.com/science/article/pii/S1364682613003337 doi: https://doi.org/10.1016/j.jastp.2013.12.015

Plaschke, F. (2016, February). ULF waves at the magnetopause. *Washington DC American Geophysical Union Geophysical Monograph Series*, *216*, 193–212. doi: 10.1002/9781119055006.ch12

Powell, K. G., Roe, P. L., Linde, T. J., Gombosi, T. I., & De Zeeuw, D. L. (1999, September). A Solution-adaptive upwind scheme for ideal magnetohy drodynamics. *Journal of Computational Physics*, *154*(2), 284–309. doi: 10.1006/jcph.1999.6299

Prokopyszyn, A. P. K., Wright, A. N., & Hood, A. W. (2021, June). Line-tied boundary conditions can cause resonant absorption models to generate unphysically large boundary layers. *Astrophysical Journal*, *914*(1), 15. doi: 10.3847/1538-4357/abf65b

Pulkkinen, A., Bernabeu, E., Thomson, A., Viljanen, A., Pirjola, R., Boteler, D., et al. (2017, July). Geomagnetically induced currents: Science, engineering, and applications readiness. *Space Weather*, *15*(7), 828–856. doi: 10.1002/2016SW001501

Radoski, H. R. (1974, February). A theory of latitude dependent geomagnetic micropulsations: The asymptotic fields. *Journal of Geophysical Research*, *79*, 595–603. doi: 10.1029/JA079i004p00595

Rae, I. J., Murphy, K. R., Watt, C. E. J., Sandhu, J. K., Georgiou, M., Degeling, A. W., et al. (2019, October). How do ultra-low frequency waves access the inner magnetosphere during geomagnetic storms? *Geophysical Research Letters*, *46*(19), 10,699–10,709. doi: 10.1029/2019GL082395

Rankin, R., Gillies, D. M., & Degeling, A. W. (2021, June). On the relationship between shear Alfvén waves, auroral electron acceleration, and field line resonances. *Space Science Reviews*, *217*(4), 60. doi: 10.1007/s11214-021-00830-x

Sakurai, T., Wright, A. N., Takahashi, K., Elsden, T., Ebihara, Y., Sato, N., et al. (2022, August). Poleward moving auroral arcs and Pc5 oscillations. *Journal of Geophysical Research (Space Physics)*, *127*(8), e30362. doi: 10.1029/2022JA030362

Salat, A., & Tataronis, J. A. (2000, June). Conditions for existence of orthogonal coordinate systems oriented by magnetic field lines. *Journal of Geophysical Research*, *105*(A6), 13055–13062. doi: 10.1029/1999ja000221

Sandhu, J. K., Rae, I. J., Staples, F. A., Hartley, D. P., Walach, M. T., Elsden, T., & Murphy, K. R. (2021, July). The roles of the magnetopause and plasmapause in storm-time ULF wave power enhancements. *Journal of Geophysical Research (Space Physics)*, *126*(7), e29337. doi: 10.1029/2021JA029337

Sandhu, J. K., Yeoman, T. K., & Rae, I. J. (2018, November). Variations of field line eigenfrequencies with ring current

intensity. *Journal of Geophysical Research (Space Physics)*, *123*(11), 9325–9339. doi: 10.1029/2018JA025751

Sarris, T. E., Li, X., Zhao, H., Papadakis, K., Liu, W., Tu, W., et al. (2022, October). Distribution of ULF wave power in magnetic latitude and local time using THEMIS and arase measurements. *Journal of Geophysical Research (Space Physics)*, *127*(10), e2022JA030469. doi: 10.1029/2022JA030469

Saur, J., Chané, E., & Hartkorn, O. (2018, January). Modeling Magneto spheric Fields in the Jupiter System. In H. Lühr, J. Wicht, S. A. Gilder, & M. Holschneider (Eds.), *Magnetic fields in the solar system*, *448*, 153–182. doi: 10.1007/978-3-319-64292-5_6

Schulz, M., & Lanzerotti, L. J. (1974). *Particle diffusion in the radiation belts*. Physics and Chemistry in Space, ISBN: 978-3-642-65677-4. Berlin: Springer. doi: 10.1007/978-3-642-65675-0

Shi, X., Baker, J. B. H., Ruohoniemi, J. M., Hartinger, M. D., Murphy, K. R., Rodriguez, J. V., et al. (2018, October). Long-lasting poloidal ULF waves observed by multiple satellites and high-latitude SuperDARN radars. *Journal of Geophysical Research (Space Physics)*, *123*(10), 8422–8438. doi: 10.1029/2018JA026003

Shi, X., Hartinger, M. D., Baker, J. B. H., Murphy, B. S., Bedrosian, P. A., Kelbert, A., & Rigler, E. J. (2022, April). Characteristics and sources of Intense geoelectric fields in the United States: Comparative analysis of multiple geomagnetic storms. *Space Weather*, *20*(4), e2021SW002967. doi: 10.1029/2021SW002967

Southwood, D. J. (1974, March). Some features of field line resonances in the magnetosphere. *Planetary Space Science*, *22*, 483–491. doi: 10.1016/0032-0633(74) 90078-6

Southwood, D. J. (1976). A general approach to low-frequency instability in the ring current plasma. *Journal of Geophysical Research*, *81*(19), 3340–3348. doi: 10.1029/JA081i019p03340

Southwood, D. J., Cao, H., Shebanits, O., Elsden, T., Hunt, G. J., & Dougherty, M. K. (2021, February). Discovery of Alfvén Waves Planetward of Saturn's Rings. *Journal of Geophysical Research (Space Physics)*, *126*(2), e28473. doi: 10.1029/2020JA028473

Southwood, D. J., Dungey, J. W., & Etherington, R. J. (1969, March). Bounce resonant interaction between pulsations and trapped particles. *Planetary and Space Science*, *17*(3), 349–361. doi: 10.1016/0032-0633(69)90068-3

Southwood, D. J., & Hughes, W. J. (1983). Theory of hydromagnetic waves in the magnetosphere. *Space Science Reviews*, *35*, 301–366. doi: 10.1007/BF00169231

Sucksdorff, E. (1939). Giant pulsations recorded at sodankylä during 1914–1938. *Journal of Geophysical Research*, *44*(2), 157–170. doi: 10.1029/TE044i002p00157

Takahashi, K., Claudepierre, S. G., Rankin, R., Mann, I. R., & Smith, C. W. (2018, June). Van Allen probes observation of a fundamental poloidal standing Alfvén wave event related to giant pulsations. *Journal of Geophysical Research (Space Physics)*, *123*(6), 4574–4593. doi: 10.1029/2017JA025139

Takahashi, K., & Denton, R. E. (2021). Nodal structure of toroidal standing Alfvén waves and its implication for field line mass density distribution. *Journal of Geophysical Research: Space Physics*, *126*(5). doi: 10.1029/2020ja028981

Takahashi, K., Denton, R. E., & Singer, H. J. (2010). Solar cycle variation of geosynchronous plasma mass density derived from the frequency of standing alfven waves. *Journal of Geophysical Research: Space Physics*, *115*, A07207. doi: ArtnA0720710.1029/2009ja015243

Takahashi, K., Glassmeier, K. H., Angelopoulos, V., Bonnell, J., Nishimura, Y., Singer, H. J., & Russell, C. T. (2011). Multisatellite observations of a giant pulsation event. *Journal of Geophysical Research: Space Physics*, *116*(A11). doi: 10.1029/2011ja016955

Takahashi, K., Hartinger, M. D., Angelopoulos, V., & Glassmeier, K.-H. (2015, August). A statistical study of fundamental toroidal mode standing Alfvén waves using THEMIS ion bulk velocity data. *Journal of Geophysical Research (Space Physics)*, *120*(8), 6474–6495. doi: 10.1002/2015JA021207

Takahashi, K., Hartinger, M. D., Angelopoulos, V., Glassmeier, K.-H., & Singer, H. J. (2013, July). Multispacecraft observations of fundamental poloidal waves without ground magnetic signatures. *Journal of Geophysical Research (Space Physics)*, *118*(7), 4319–4334. doi: 10.1002/jgra.50405

Takahashi, K., & Heilig, B. (2019, August). L versus time structures of dayside magnetic pulsations detected by the European quasi-meridional magnetometer array. *Journal of Geophysical Research (Space Physics)*, *124*(8), 6566–6584. doi: 10.1029/2019JA026796

Takahashi, K., Lee, D.-H., Merkin, V. G., Lyon, J. G., & Hartinger, M. D. (2016, October). On the origin of the dawn-dusk asymmetry of toroidal Pc5 waves. *Journal of Geophysical Research (Space Physics)*, *121*(10), 9632–9650. doi: 10.1002/2016JA023009

Takahashi, K., Lysak, R., & Vellante, M. (2022, September). Statistical analysis of Pi2 pulsations observed by Van Allen probes. *Journal of Geophysical Research (Space Physics)*, *127*(9), e30674. doi: 10.1029/2022JA030674

Takahashi, K., Lysak, R., Vellante, M., Kletzing, C. A., Hartinger, M. D., & Smith, C. W. (2018, March). Observation and numerical simulation of cavity mode oscillations excited by an interplanetary shock. *Journal of Geophysical Research (Space Physics)*, *123*(3), 1969–1988. doi: 10.1002/2017JA024639

Takahashi, K., & McPherron, R. L. (1984, November). Standing hydromagnetic oscillations in the magnetosphere. *Planetary and Space Science*, *32*, 1343–1359.

Takahashi, K., Oimatsu, S., Nosé, M., Min, K., Claudepierre, S. G., Chan, A., et al. (2018, January). Van Allen probes observations of second harmonic poloidal standing Alfvén waves. *Journal of Geophysical Research (Space Physics)*, *123*(1), 611–637. doi: 10.1002/2017JA024869

Takahashi, K., Sato, N., Warnecke, J., Lühr, H., Spence, H. E., & Tonegawa, Y. (1992). On the standing wave mode of giant pulsations. *Journal of Geophysical Research*, *97*(A7), 10717. doi: 10.1029/92ja00382

Tsyganenko, N. A. (1989). A magnetospheric magnetic field model with a warped tail current sheet. *Planetary and Space Science*, *37*(1), 5–20. doi: 10.1016/0032-0633(89)90066-4

Tsyganenko, N. A. (2002). A model of the near magnetosphere with a dawn-dusk asymmetry 2. parameterization and fitting to observations. *Journal of Geophysical Research: Space Physics*, *107*(A8), SMP 10-1–SMP 10-17. doi: 10.1029/2001ja000220

Tsyganenko, N. A., & Sitnov, M. I. (2005, March). Modeling the dynamics of the inner magnetosphere during strong geomagnetic storms. *Journal of Geophysical Research (Space Physics)*, *110*(A3), A03208. doi: 10.1029/2004JA010798

Tóth, G., Sokolov, I. V., Gombosi, T. I., Chesney, D. R., Clauer, C. R., De Zeeuw, D. L., et al. (2005). Space weather modeling framework: A new tool for the space science community. *Journal of Geophysical Research: Space Physics*, *110*(A12). Retrieved from https://agupubs.onlinelibrary.wiley.com/doi/abs/10.1029/2005JA011126 doi: https://doi.org/10.1029/2005JA011126

Vellante, M., Piersanti, M., & Pietropaolo, E. (2014). Comparison of equatorial plasma mass densities deduced from field line resonances observed at ground for dipole and IGRF models. *Journal of Geophysical Research: Space Physics*, *119*(4), 2623–2633. doi: 10.1002/2013ja019568

Verkhoglyadova, O. P., Meng, X., Mannucci, A. J., & McGranaghan, R. M. (2018). Semianalytical estimation of energy deposition in the ionosphere by monochromatic Alfvén waves. *Journal of Geophysical Research: Space Physics*, *123*(6), 5210–5222. Retrieved from https://agupubs.onlinelibrary.wiley.com/doi/abs/10.1029/2017JA025097 doi: https://doi.org/10.1029/2017JA025097

Wang, B., Liu, T., Nishimura, Y., Zhang, H., Hartinger, M., Shi, X., et al. (2020, December). Global propagation of magnetospheric Pc5 ULF waves driven by foreshock transients. *Journal of Geophysical Research (Space Physics)*, *125*(12), e28411. doi: 10.1029/2020JA028411

Wang, B., Nishimura, Y., Hietala, H., & Angelopoulos, V. (2022, November). Investigating the role of magnetosheath high-speed jets in triggering dayside ground magnetic ultra-low frequency waves. *Geophysical Research Letters*, *49*(22), e2022GL099768. doi: 10.1029/2022GL099768

Wang, C.-P., Takahashi, K., Xing, X., & Bortnik, J. (2022, May). Plasmas-pheric Pi2 pulsation enhancement in response to plasma sheet Pi2 wave source: Statistical study using Van Allen probes and THEMIS conjunctions. *Journal of Geophysical Research (Space Physics)*, *127*(5), e30399. doi: 10.1029/2022JA030399

Waters, C. L., & Cox, S. P. (2009, July). ULF wave effects on high frequency signal propagation through the ionosphere. *Annales Geophysicae*, *27*(7), 2779–2788. doi: 10.5194/angeo-27-2779-2009

Waters, C. L., Menk, F. W., & Fraser, B. J. (1991). The resonance structure of low latitude Pc3 geomagnetic-pulsations. *Geophysical Research Letters*, *18*(12), 2293–2296. doi: 10.1029/91gl02550

Wharton, S. J., Rae, I. J., Sandhu, J. K., Walach, M. T., Wright, D. M., & Yeoman, T. A. K. (2020, June). The changing eigenfrequency continuum during geomagnetic storms: Implications for plasma mass dynamics and ULF wave coupling. *Journal of Geophysical Research (Space Physics)*, *125*(6), e27648. doi: 10.1029/2019JA027648

Wharton, S. J., Wright, D. M., Yeoman, T. K., James, M. K., & Sandhu, J. K. (2018, August). Cross-phase determination of ultralow frequency wave harmonic frequencies and their

associated plasma mass density distributions. *Journal of Geophysical Research (Space Physics)*, *123*(8), 6231–6250. doi: 10.1029/2018JA025487

Wright, A. N., & Allan, W. (2008, February). Simulations of Alfvén waves in the geomagnetic tail and their auroral signatures. *Journal of Geophysical Research (Space Physics)*, *113*(A2), A02206. doi: 10.1029/2007JA012464

Wright, A. N., Degeling, A. W., & Elsden, T. (2022). Resonance maps for 3D Alfvén waves in a compressed dipole field. *Journal of Geophysical Research: Space Physics*, *127*(4), e2022JA030294. doi: 10.1029/2022JA030294

Wright, A. N., & Elsden, T. (2016, December). The theoretical foundation of 3D Alfvén resonances: Normal modes. *Astrophysical Journal*, *833*, 230. doi: 10.3847/1538-4357/833/2/230

Wright, A. N., & Elsden, T. (2020, February). Simulations of MHD wave propagation and coupling in a 3-D magnetosphere. *Journal of Geophysical Research (Space Physics)*, *125*(2), e27589. doi: 10.1029/2019JA027589

Wright, A. N., Elsden, T., & Takahashi, K. (2018, August). Modeling the dawn/dusk asymmetry of field line resonances. *Journal of Geophysical Research (Space Physics)*, *123*(8), 6443–6456. doi: 10.1029/2018JA025638

Wright, A. N., & Mann, I. R. (2006, January). Global MHD Eigenmodes of the Outer Magnetosphere. In *Magnetospheric ulf waves: Synthesis and new directions* (Vol. 169, p. 51). doi: 10.1029/169GM06

Wright, A. N., & Southwood, D. J. (1987, February). Stationary Alfvénic structures. *Journal of Geophysical Research*, *92*(A2), 1167–1176. doi: 10.1029/JA092iA02p01167

Wright, A. N., & Thompson, M. J. (1994, March). Analytical treatment of Alfvén resonances and singularities in nonuniform magnetoplasmas. *Physics of Plasmas*, *1*, 691–705. doi: 10.1063/1.870815

Wright, D. M., & Yeoman, T. K. (1999). CUTLASS observations of a high-*m* ULF wave and its consequences for the DOPE HF Doppler sounder. *Annales Geophysicae*, *17*(11), 1493–1497. doi: 10.1007/s00585-999-1493-3

Yagova, N. V., Pilipenko, V. A., Sakharov, Y. A., & Selivanov, V. N. (2021, December). Spatial scale of geomagnetic Pc5/Pi3 pulsations as a factor of their efficiency in generation of geomagnetically induced currents. *Earth, Planets and Space*, *73*(1), 88. doi: 10.1186/s40623-021-01407-2

Yamakawa, T., Seki, K., Amano, T., Miyoshi, Y., Takahashi, N., Nakamizo, A., & Yamamoto, K. (2022). Excitation of two types of storm-time Pc5 ULF waves by ring current ions based on the magnetosphere-ionosphere coupled model. *Journal of Geophysical Research: Space Physics*, *127*(8), e2022JA030486. Retrieved from https://agupubs.onlinelibrary.wiley.com/doi/abs/10.1029/2022JA030486 (e2022JA030486 2022JA030486) doi: https://doi.org/10.1029/2022JA030486

Yamakawa, T., Seki, K., Amano, T., Takahashi, N., & Miyoshi, Y. (2019). Excitation of storm time Pc5 ULF waves by ring current ions based on the drift-kinetic simulation. *Geophysical Research Letters*, *46*(4), 1911–1918. Retrieved from https://agupubs.onlinelibrary.wiley.com/doi/abs/10.1029/2018GL081573 doi: https://doi.org/10.1029/2018GL081573

Yamakawa, T., Seki, K., Amano, T., Takahashi, N., & Miyoshi, Y. (2020). Excitation of internally driven ulf waves by the drift-bounce resonance with ring current ions based on the drift-kinetic simulation. *Journal of Geophysical Research: Space Physics*, *125*(11), e2020JA028231. Retrieved from https://agupubs.onlinelibrary.wiley.com/doi/abs/10.1029/2020JA028231 (e2020JA028231 2020JA028231) doi: https://doi.org/10.1029/2020JA028231

Yamamoto, K., Nosé, M., Kasahara, S., Yokota, S., Keika, K., Matsuoka, A., et al. (2018). Giant pulsations excited by a steep earthward gradient of proton phase space density: Arase observation. *Geophysical Research Letters*, *45*(14), 6773–6781. doi: 10.1029/2018gl078293

Yang, B., Zong, Q. G., Fu, S. Y., Li, X., Korth, A., Fu, H. S., et al. (2011). The role of ULF waves interacting with oxygen ions at the outer ring current during storm times. *Journal of Geophysical Research: Space Physics*, *116*(A1). doi: 10.1029/2010ja015683

Yang, Z., Zhang, B., Lotko, W., Sorathia, K. A., Pham, K., Luan, X., et al. (2022, September). Formation of Alfvén wave ducts by magnetotail flow bursts. *Journal of Geophysical Research (Space Physics)*, *127*(9), e30841. doi: 10.1029/2022JA030841

Yeoman, T. K., & Wright, D. M. (2001). ULF waves with drift resonance and drift-bounce resonance energy sources as observed in artificially-induced HF radar backscatter. *Annales Geophysicae*, *19*(2), 159–170. doi: 10.5194/angeo-19-159-2001

Zhang, B., Lotko, W., Brambles, O., Damiano, P., Wiltberger, M., & Lyon, J. (2012, September). Magnetotail origins of auroral Alfvénic power. *Journal of Geophysical Research (Space Physics)*, *117*(A9), A09205. doi: 10.1029/2012JA017680

Zhao, X. X., Hao, Y. X., Zong, Q.-G., Zhou, X.-Z., Yue, C., Chen, X. R., et al. (2020). Origin of electron boomerang stripes: Localized ulf wave-particle interactions. *Geophysical Research Letters*, *47*(17), e2020GL087960. Retrieved from https://agupubs.onlinelibrary.wiley.com/doi/abs/10.1029/2020GL087960 (e2020GL087960 10.1029/2020GL087960) doi: https://doi.org/10.1029/2020GL087960

Zong, Q., Rankin, R., & Zhou, X. (2017, December). The interaction of ultra-low-frequency pc3-5 waves with charged particles in Earth's magnetosphere. *Reviews of Modern Plasma Physics*, *1*(1), 10. doi: 10.1007/s41614-017-0011-4